Chem

CellPress

Article

Fusobacterium nucleatum-mimicking nanovehicles to overcome chemoresistance for breast cancer treatment by eliminating tumor-colonizing bacteria

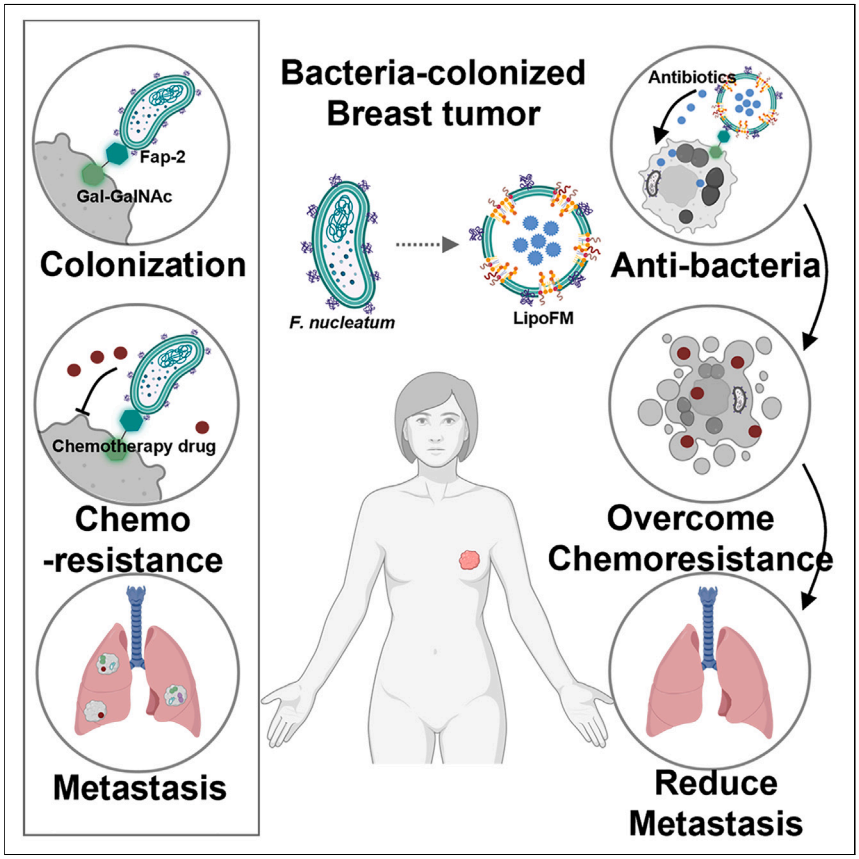

F. nucleatum in human breast cancer correlates with D-galactose-β(1-3)-N-acetyl-D-galactosamine on tumor cells and chemoresistance. *F. nucleatum*-mimicking nanovehicles (LipoFM) developed here could effectively target tumors, deliver antibiotics, eradicate intratumoral microbiomes, inhibit cancer metastasis, and improve chemotherapy efficacy.

Linfu Chen, Jingjing Shen, Zheyu Kang, ..., Yang Yang, Zhuang Liu, Qian Chen

chenqian@suda.edu.cn

Highlights

Tumor-targeting LipoFM developed by fusing *F. nucleatum* membrane with liposome

Antibiotics loaded LipoFM selectively eradicating tumor-resident *F. nucleatum*

Selective disruption of tumor-colonizing bacteria improving cancer treatment

A promising targeted drug delivery carrier for bacteria-colonized tumors

Chen et al., Chem *10*, 1783–1803
June 13, 2024
https://doi.org/10.1016/j.chempr.2024.01.030

Chem

CellPress

Article

Fusobacterium nucleatum-mimicking nanovehicles to overcome chemoresistance for breast cancer treatment by eliminating tumor-colonizing bacteria

Linfu Chen,[1,6] Jingjing Shen,[1,6] Zheyu Kang,[1] Zemin Zhang,[2] Zixuan Zheng,[2] Lin Zhang,[3] Zhisheng Xiao,[1] Qiang Zhang,[2,5] Huapan Fang,[1] Jun Zhou,[1] Yudong Wang,[3] Yang Yang,[2,4,5] Zhuang Liu,[1] and Qian Chen[1,7,*]

SUMMARY

Herein, we discovered that the tumor-colonized *F. nucleatum* is closely correlated with the expression of D-galactose-β(1-3)-N-acetyl-D-galactosamine (Gal-GalNAc) in breast cancer and would promote chemoresistance. Therefore, we designed *F. nucleatum*-mimicking nanovehicles by fusing the *F. nucleatum* cytoplasmic membrane (FM) with antibiotic-loaded liposomes and found that the obtained nanovehicles (Colistin-LipoFM) could selectively eradicate tumor-resident *F. nucleatum* and significantly restore chemotherapy efficacy. In addition, our *F. nucleatum*-mimicking nanovehicles, containing a broad-spectrum antibiotic, could interfere with other intratumoral microbiomes to inhibit the lung metastasis of breast cancer and further promote the efficacy of standard clinically used breast cancer chemotherapy, leading to complete regression of established tumors in some mice. Therefore, the *F. nucleatum*-mimicking nanovehicles should be an excellent targeted drug delivery carrier for tumors colonized with bacteria and provide a promising possibility to promote existing cancer therapies by selectively killing tumor-colonizing bacteria.

INTRODUCTION

Despite the progress of modern medicine, breast cancer remains the most common malignant disease and represents the primary cause of cancer-related deaths among women.[1–4] With the widespread implementation of mammographic screening, the incidence of breast cancer is still increasing steadily.[4,5] Although many patients miss the optimal timing for surgery due to the late stage of diagnosis,[6] more than 30% of patients with even early-stage disease eventually develop metastasis.[7,8] Chemotherapy, especially combination chemotherapy, remains the gold-standard strategy in cancer treatment due to its multifaceted mechanism of shrinking tumor size, reducing tumor growth, and inhibiting tumor metastasis.[9,10] However, chemoresistance eventually develops and leads to the recurrence of cancer cells, and the five-year survival rate is unfortunately less than 30% in advanced breast cancer patients.[11–13] Thus, chemotherapy resistance represents the major obstacle in the treatment of breast cancer, and the 'battle' against it should be enduring.[14]

Recently, some studies have demonstrated that the microbiota, including the tumor microbiome, perform critical roles in cancer progression and therapeutic responses.[15–18] *Fusobacterium nucleatum* (*F. nucleatum*), a Gram-negative anaerobic

THE BIGGER PICTURE

A significant presence of *F. nucleatum* was observed in human breast cancer. Its colonization closely correlates with the expression of Gal-GalNAc on tumor cells, thereby facilitating chemoresistance. To address this, *F. nucleatum*-mimicking nanovehicles (LipoFM) were developed by combining the *F. nucleatum* membrane (FM) with liposomes, demonstrating superior tumor targeting. Colistin loaded into LipoFM could selectively eradicate intratumoral *F. nucleatum*, thereby improving chemotherapy efficacy. Additionally, Doxycycline-loaded LipoFM (Doxy-LipoFM) can disrupt other intratumoral microbiomes implicated in breast cancer metastasis. Notably, Doxy-LipoFM could inhibit lung metastasis and improve the efficacy of chemotherapy, leading to complete tumor regression. Therefore, LipoFM emerges as a promising targeted drug delivery carrier for bacteria-colonized tumors, offering potential enhancements to existing cancer therapies through the selective elimination of tumor-colonizing bacteria.

bacterium, is abundant in colorectal cancer and has been found to be closely associated with the formation of pro-tumor microenvironment to promote resistance to chemotherapy.[19–21] In addition to colorectal cancer, *F. nucleatum* has also been found in breast cancer samples, especially in those with high expression of D-galactose-β(1-3)-N-acetyl-D-galactosamine (Gal-GalNAc).[22] Therefore, it is important to investigate whether *F. nucleatum* can induce chemoresistance to breast cancer and, if yes, to further explore the possibility of overcoming chemoresistance in breast tumors by selectively eliminating tumor-colonizing bacteria.[23]

Herein, we demonstrated that in comparison with paracancerous tissues and normal tissues, human breast cancer samples obtained from the same patients showed high levels of *F. nucleatum* colonization. Moreover, it was found that the abundance of *F. nucleatum* was positively correlated with the level of Gal-GalNAc, owing to the interactions between membrane protein Fap-2 in *F. nucleatum* and Gal-GalNAc expressed on the surface of breast tumor cells. We also demonstrated that breast tumors colonized with *F. nucleatum* exhibited significant resistance to different chemotherapeutic drugs, possibly due to the activated autophagy pathway of breast cancer cells to reduce their responses to chemotherapeutics. To overcome *F. nucleatum*-induced chemoresistance to breast cancer, we developed *F. nucleatum*-mimicking nanovehicles by fusing liposomes with the *F. nucleatum* cytoplasmic membrane (FM) (LipoFM). Interestingly, the obtained LipoFM exhibited superior tumor-specific targeting and retention due to the binding of FM with Gal-GalNAc overexpressed on tumor cells (Figure 1A). After encapsulation with the antibiotic colistin, our nanovehicle successfully restored the therapeutic efficacy of chemotherapy in an *F. nucleatum*-infected mouse breast tumor model. As breast cancer is known to have a diverse microbiome that promotes cancer cell survival and metastasis,[24] we further demonstrated that LipoFM loaded with a broad-spectrum antibiotic, Doxycycline (Doxy), could interfere with the intratumoral microflora and inhibit the lung metastasis of breast cancer infected with a mixture of different bacteria. Notably, Doxy-LipoFM could remarkably improve the therapeutic efficacy of the standard chemotherapy CMF (cyclophosphamide, methotrexate, and 5-fluorouracil) for breast cancer,[25] achieving outstanding therapeutic effects in the breast tumor model infected with a mixture of different bacteria and complete regression of established tumors in some mice (Figure 1B). Thus, antibiotic-loaded *F. nucleatum*-mimicking nanovehicles exhibit great potential to overcome chemoresistance of breast cancer and might inspire future chemotherapy strategies for breast tumors colonized with bacteria.

RESULTS AND DISCUSSION

Intratumor colonization of *F. nucleatum* in human breast cancer

To investigate the colonization condition of *F. nucleatum* in patients with breast cancer, breast tumor tissues, paired paracancer tissues together with normal breast tissues, were collected to analyze the microbiome composition (Figure 2A; Table S1). To exclude the effect of laboratory-borne contaminants, we introduced the samples of environmental background control (EBC) and non-template control (NTC). To quantify the biomass of tissue microbiota, a real-time quantitative polymerase chain reaction (qPCR) assay with universal primers specific for the bacteria was carried out. The levels of bacterial DNA in all breast tumor tissues were significantly higher than those in both paracancer tissues and normal breast tissues, reaching ~188 equivalent bacteria/100 ng of DNA (Figure 2B). To further characterize the composition of the intratumoral microbiome, 5R 16S rRNA sequencing was performed to evaluate the overall microbiome of breast tumors, paired paracancerous tissues, and

[1]Institute of Functional Nano and Soft Materials (FUNSOM), Jiangsu Key Laboratory for Carbon-Based Functional Materials and Devices, Soochow University, Suzhou 215123, P.R. China

[2]Department of Thoracic Surgery, Shanghai Pulmonary Hospital, Tongji University School of Medicine, Shanghai 200433, P.R. China

[3]Department of Gynecologic Oncology, the International Peace Maternity and Child Health Hospital, School of Medicine, Shanghai Jiao Tong University, Shanghai 200030, P.R. China

[4]Central Laboratory, Shanghai Pulmonary Hospital, School of Medicine, Tongji University, Shanghai 200433, P.R. China

[5]School of Materials Science and Engineering, Tongji University, Shanghai 201804, P.R. China

[6]These authors contributed equally

[7]Lead contact

*Correspondence: chenqian@suda.edu.cn

https://doi.org/10.1016/j.chempr.2024.01.030

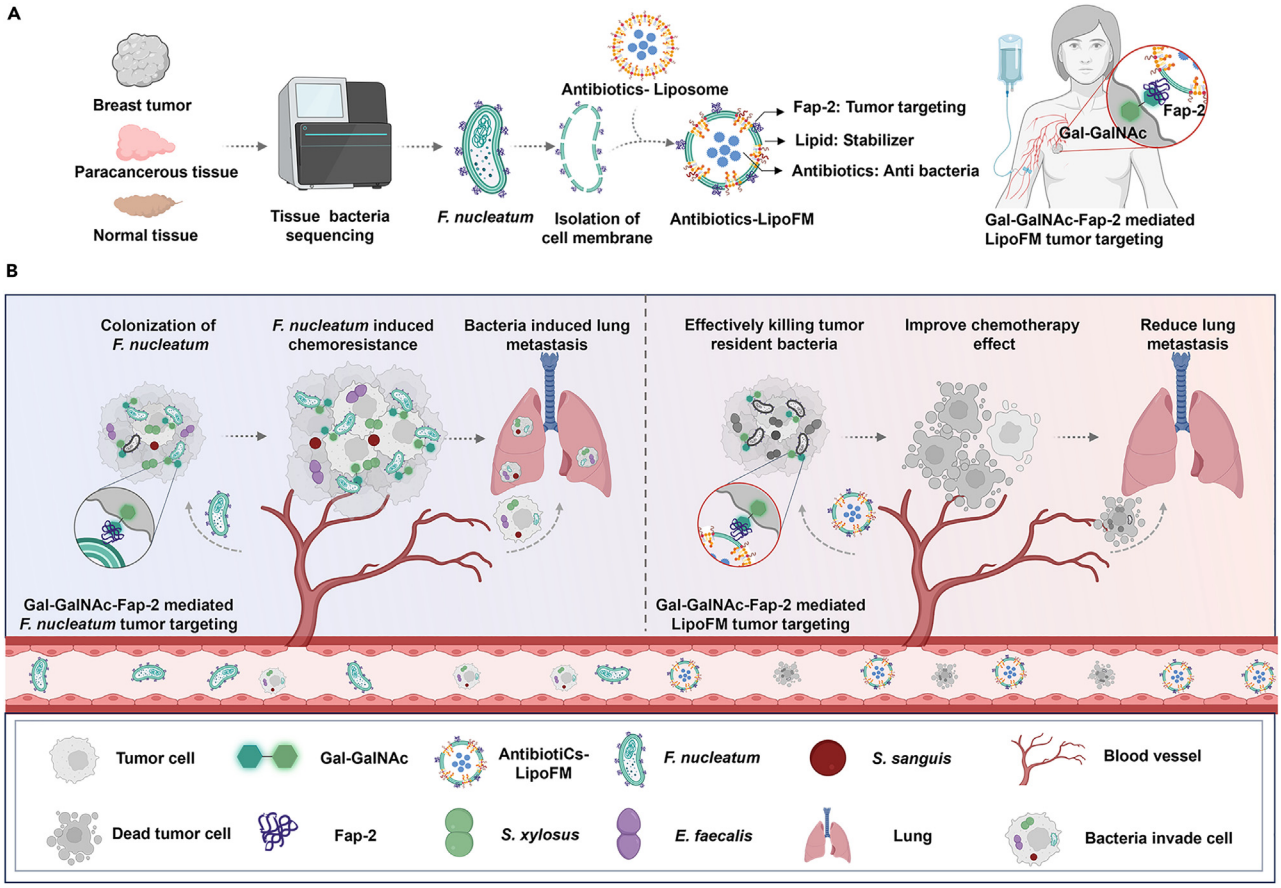

Figure 1. *F. nucleatum*-mimicking nanovehicles overcome chemoresistance of breast cancer by eliminating tumor-colonizing bacteria

(A) *F. nucleatum* was identified as one of the most enriched bacteria in breast tumor tissues, and *F. nucleatum*-mimicking nanovehicles were prepared by fusing the *F. nucleatum* cytoplasmic membrane and antibiotic-loaded liposomes to achieve targeted elimination of breast cancer colonized bacteria to enhance chemotherapy efficacy.

(B) The obtained antibiotic LipoFM could effectively interfere with the other intratumoral microflora, inhibiting the lung metastasis of breast cancer infected by different types of bacteria, and significantly improve the therapeutic efficacy of the standard chemotherapy for breast cancer.

normal breast tissues.[15] Differential analysis of the dominant community showed that *Cyanobacteria*, *Verrucomicrobia*, *F. nucleatum*, *Proteobacteria*, and *Bacteroidetes* were enriched in breast tumor tissues, whereas the *Thermi*, *Chloroflexi*, *Actinobacteria*, and *Firmicutes* were relatively less (Figure 2C). Considering that *F. nucleatum* has the ability to promote tumor growth and metastasis, induce immunosuppressive tumor microenvironment, and facilitate chemoresistance,[19–21,23,26,27] we then quantified the relative abundance of *F. nucleatum* using the above paired cohort in more detail. It was observed that 5 of 8 snap-frozen clinical primary breast tumor samples were positive for *F. nucleatum* (P1, P2, P3, P6, and P7), and 2 of 8 (P1 and P2) had more than 1% *F. nucleatum* abundance (Figures 2D and 2E). In addition, ~1.4% of *F. nucleatum* was detected in *F. nucleatum*-positive tumors, which was nearly 8-fold higher and 18-fold higher than that in matched paracancerous tissues and normal breast tissues (Figure 2F).

It was reported in previous studies that the specific attachment and colonization of *F. nucleatum* in breast tumors is facilitated by high expression of Gal-GalNAc on the membrane of breast cancer cells.[22] We thus analyzed the level of Gal-GalNAc in formalin-fixed paraffin-embedded (FFPE) tumor tissues and matched paracancerous

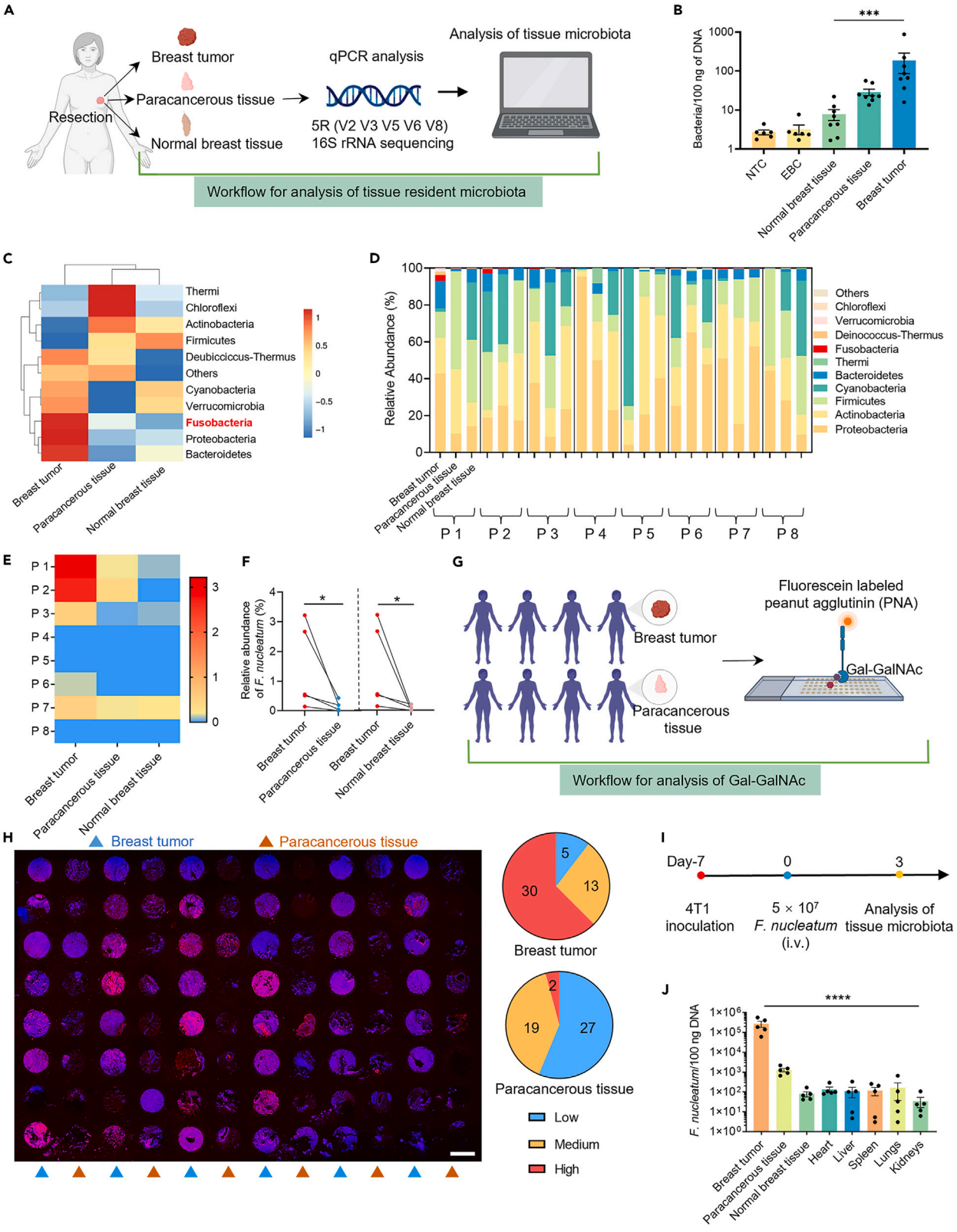
A
Breast tumor
Paracancerous tissue
Normal breast tissue
Resection
qPCR analysis
5R (V2 V3 V5 V6 V8)
16S rRNA sequencing
Analysis of tissue microbiota
Workflow for analysis of tissue resident microbiota
B
***
Bacteria/100 ng of DNA
NTC
EBC
Normal breast tissue
Paracancerous tissue
Breast tumor
C
Thermi
Chloroflexi
Actinobacteria
Firmicutes
Deubicciccus-Thermus
Others
Cyanobacteria
Verrucomicrobia
Fusobacteria
Proteobacteria
Bacteroidetes
Breast tumor
Paracancerous tissue
Normal breast tissue
D
Relative Abundance (%)
Others
Chloroflexi
Verrucomicrobia
Deinococcus-Thermus
Fusobacteria
Thermi
Bacteroidetes
Cyanobacteria
Firmicutes
Actinobacteria
Proteobacteria
P 1
P 2
P 3
P 4
P 5
P 6
P 7
P 8
E
F
Relative abundance of F. nucleatum (%)
G
Fluorescein labeled peanut agglutinin (PNA)
Breast tumor
Paracancerous tissue
Gal-GalNAc
Workflow for analysis of Gal-GalNAc
H
Breast tumor
Paracancerous tissue
5
13
30
Breast tumor
2
19
27
Paracancerous tissue
Low
Medium
High
I
Day-7
0
3
4T1 inoculation
5 × 10⁷ F. nucleatum (i.v.)
Analysis of tissue microbiota
J
****
F. nucleatum/100 ng DNA
Heart
Liver
Spleen
Lungs
Kidneys

Figure 2. The abundance of *F. nucleatum* in breast tumors

(A) Schematic diagram showing the workflow for qPCR quantification and 5R 16S RNA sequencing of tissue resident microbiota.

(B) qPCR quantification of microbiota in human breast tumors (n = 8), paracancerous tissues (n = 8), normal breast tissues (n = 8), environment background control (EBC) (n = 6), and non-template control (NTC) (n = 6). Data are presented as the mean ± SEM.

(C) Heatmap showing the relative abundance of the tumor microbiome in different groups. Phylum-level taxonomy is presented.

(D) Phylum-level microbial composition of paired breast primary tumors, paracancerous tissue, and normal breast tissue.

(E) Heatmap showing the abundance of *F. nucleatum* in human breast tumor, paracancerous tissue, and normal breast tissue at phylum-level.

(F) The abundance of *F. nucleatum* in *F. nucleatum*-positive tumors and their paired paracancerous tissue and normal breast tissue.

(G) Schematic diagram showing the workflow for detecting the expression of Gal-GalNAc in human breast tumors and paired paracancerous tissue.

(H) Images of immunofluorescence staining of Gal-GalNAc in breast tumors (n = 48) and paracarcinoma tissue sections (n = 48) collected from patients with breast tumors (left). Scale bars, 1,500 μm. Red fluorescence represents Gal-GalNAc. Statistical analysis of the mean intensity of Gal-GalNAc (high, mean intensity > 8.994; medium, mean intensity > 1.974; low, mean intensity <1.974) (right).

(I) Schematic illustrating the design of animal experiments in 4T1 tumor-bearing mice.

(J) *F. nucleatum* gene copy number in breast tumors, paracancerous tissues, normal breast tissues, hearts, livers, spleens, lungs, and kidneys of mice after i.v. injection with 5×10^7 *F. nucleatum* determined by qPCR. Data are presented as the mean ± SEM (n = 5). Statistical significance was calculated via the Mann-Whitney test (B and F) or one-way ANOVA (J) in GraphPad Prism. *p < 0.05; **p < 0.01; ***p < 0.001; ****p < 0.0001.

tissue from patients with breast cancer (n = 48) using fluorescein isothiocyanate (FITC)-labeled peanut agglutinin (PNA), a Gal-GalNAc-specific lectin (Figure 2G). As shown in Figure 2H, most breast tumor samples (30 out of 48) exhibited high expression of Gal-GalNAc, whereas high expression of Gal-GalNAc was observed only in two paracancerous tissues. Therefore, the high expression of Gal-GalNAc in breast tumors may lead to the colonization of *F. nucleatum* in breast cancer tissues.

Inspired by the tendency of *F. nucleatum* to colonize breast tumors in patients, we then investigated the migration of *F. nucleatum* in a preclinical mouse breast tumor model. Mice bearing 4T1 breast tumors were intravenously (i.v.) injected with *F. nucleatum* with the dose of 5×10^7 colony-forming units (CFUs). 72 h later, the breast tumors, paracancerous tissue, normal breast tissue, and other major organs were harvested for qPCR analysis. In line with the human data, the abundance of *F. nucleatum* was significantly higher in 4T1 tumors than in paracancerous tissues and normal breast tissues. Interestingly, nearly no *F. nucleatum* was detected in the other major organs, including the heart, liver, spleen, kidney, and lung (Figures 2I and 2J). The behavior of *F. nucleatum* within the tumor was further assessed through plate counting. The abundance of *F. nucleatum* within the tumors gradually increased over time, indicating the successful colonization of *F. nucleatum* within the 4T1 tumors (Figure S1).

F. nucleatum colonized in breast cancer would promote chemoresistance

According to previous literature, the abundance of *F. nucleatum* in colorectal cancer was closely associated with patients' clinicopathological characteristics, especially chemoresistance.[19,28] Thus, we investigated whether *F. nucleatum* could promote breast cancer cell resistance to chemotherapy. First, 4T1 mouse breast cancer cells, MCF-7 human breast epithelial luminal cancer cells, and MDA-MB-231 human highly aggressive triple-negative breast cancer cells were incubated with *F. nucleatum* at varying multiplicities of *F. nucleatum* infection ranging from 0–2,000 (MOI of *F. nucleatum*:cells). After co-culturing for 24 h, the viability of cells was determined via methyl thiazolyl tetrazolium assay. As shown in Figure S2, with the concentration of *F. nucleatum* increased, the proliferation of 4T1 cells, MCF-7 cells, and MDA-MB-231 cells was also increased. To eliminate the impact of *F. nucleatum* to cancer cell proliferation, *F. nucleatum* with the MOI at 200 was chosen to assess its role in inducing chemoresistance. Next, *F. nucleatum*-infected 4T1 cells, MCF-7 cells, and MDA-MB-231 cells (MOI = 200) were incubated with varying concentrations of chemotherapeutic drugs, such as 5-fluorouracil (5Fu) and Oxaliplatin (OXA). As

shown in Figure S3, the therapeutic effect of different chemotherapeutic drugs was significantly reduced in *F. nucleatum*-infected breast cancer cells, indicating that *F. nucleatum* could induce chemoresistance in breast cancer cells. Then, the apoptosis process of 4T1 cells after different treatments was investigated by flow cytometry. As expected, 5Fu and OXA indeed could induce the apoptosis of 4T1 cells. However, the *F. nucleatum* infection reduced the apoptosis of 4T1 cells induced by 5Fu and OXA (Figures 3A, S4, and S5). Moreover, the Western blotting results revealed that 5Fu and OXA induced the cleavage of caspase 3 (c-caspase 3) in 4T1 cells, which serves as a biomarker for apoptosis,[29] but these effects were found to be inhibited by *F. nucleatum* (Figures 3B and S6). Thus, *F. nucleatum* could impair the apoptosis process of breast cancer cells induced by chemotherapeutic drugs.

Subsequently, we proceeded to investigate the chemoresistance induced by *F. nucleatum* in mice. First, BALB/c mice bearing 4T1 tumors were intratumarally (i.t.) injected with *F. nucleatum* with the dose of 1×10^6 CFU, 1×10^7 CFU, 1×10^8 CFU, and 1×10^9 CFU on day 0. It was found that *F. nucleatum* with the injection dose at 1×10^8 CFU could promote the growth of tumors (Figure S7). Notably, with the injection dose of *F. nucleatum* increase to 1×10^9 CFU, obvious tumor necrosis was observed (Figure S8). Moreover, *F. nucleatum* with the injection dose at 1×10^6 CFU and 1×10^7 CFU could obviously induce chemoresistance (Figures 3C and 3D). Therefore, 1×10^7 CFU of *F. nucleatum* was chosen in our subsequent experiments. Similar therapeutic results were also observed in human MDA-MB-231 breast tumors (Figures 3E and S9). In addition to 5Fu, *F. nucleatum* infection also significantly affected the therapeutic effect of OXA (Figure S10). 14 days later, 4T1 breast tumors of mice with different treatments were harvested for immunohistochemical analysis. The hematoxylin and eosin (H&E) staining images indicated that tumors collected from mice treated with 5Fu + *F. nucleatum* showed obviously reduced cell damage (Figure S11). For a more detailed study, the collected tumors were processed for terminal deoxynucleotidyl transferase dUTP nick end labeling (TUNEL) and c-caspase three staining. As shown in Figure S11, the apoptosis of tumors in the 5Fu + *F. nucleatum* group was also obviously reduced, further indicating that *F. nucleatum* seriously affected the effectiveness of chemotherapy.

According to previous work, *F. nucleatum* could activate the autophagy pathway by targeting specific microRNAs and innate immune signaling to induce chemoresistance to colorectal cancer.[19] Based on this, we hypothesized that *F. nucleatum* may promote chemoresistance in breast tumors by modulating autophagy. To investigate the autophagy of breast cancer cells, immunohistochemical analysis of LC3, which is a typical autophagosome marker,[30] was performed to evaluate the autophagy of 4T1 tumors after incubation with *F. nucleatum*. As shown in Figure S12, the expression of LC3 protein in the tumors collected from mice in the 5Fu + *F. nucleatum*-treated group was obviously higher than that in the untreated and 5Fu groups. Then, different assays related to autophagy function in 4T1 cells cocultured with *F. nucleatum* were carried out. As shown in Figure 3F, the expression of LC3 in *F. nucleatum*-infected 4T1 cells was obviously increased, and the level of LC3 was related to the concentration of *F. nucleatum*. The autophagy of 4T1 cells infected with *F. nucleatum* was further assessed by transmission electron microscopy (TEM) imaging. As shown in Figure 3G, obvious autophagic vesicles were clearly observed in 4T1 cells after *F. nucleatum* infection, indicating that *F. nucleatum* infection could induce autophagy in breast cancer cells. To further validate that *F. nucleatum* promoted 4T1 cells chemoresistance by modulating autophagy, 4T1 cells infected with *F. nucleatum* were incubated with 5Fu or OXA in the presence of chloroquine (CQ), a known autophagy lysosomal inhibitor. As shown in

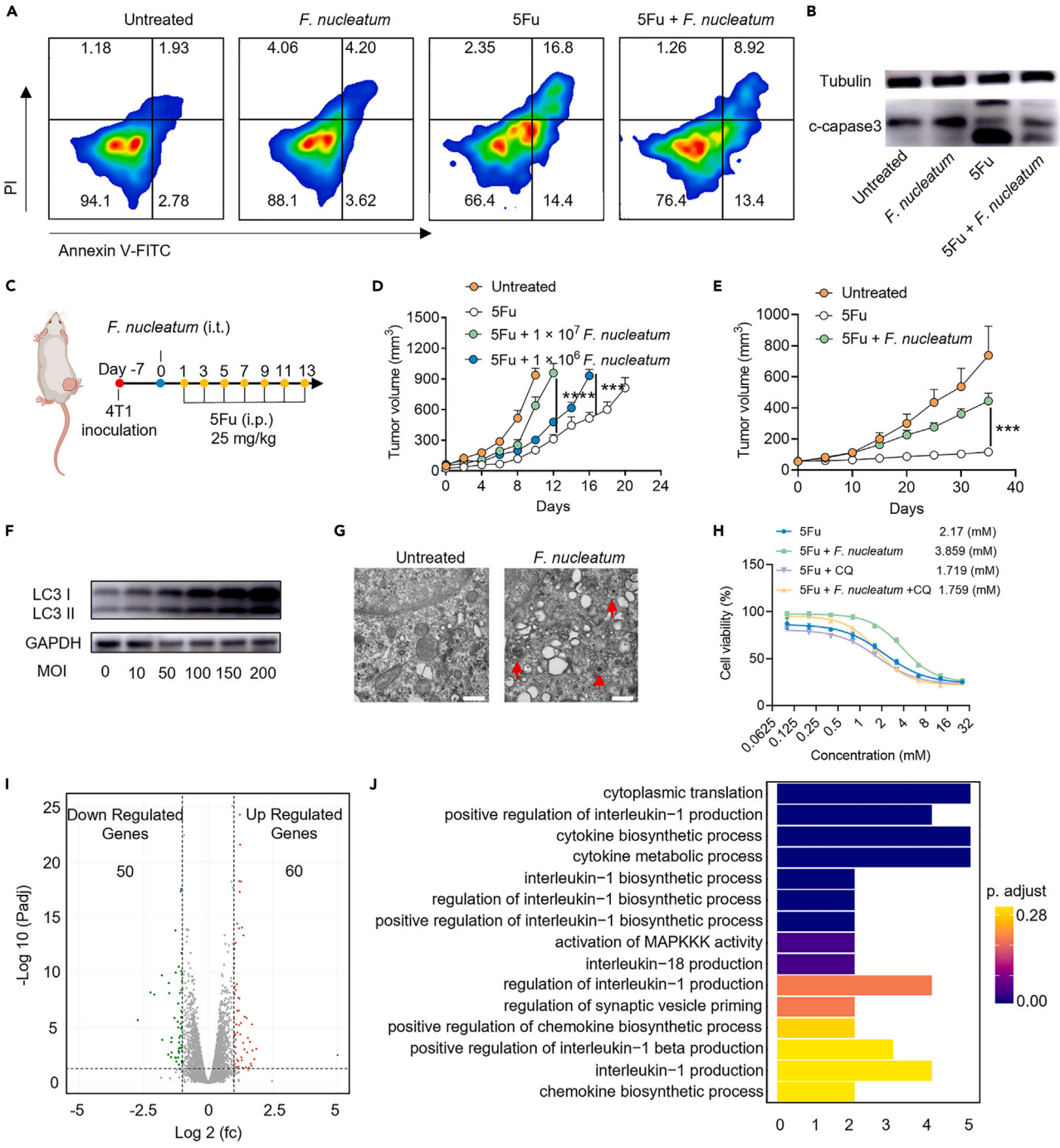

Figure 3. Breast tumor-resident *F. nucleatum* promotes chemoresistance

(A) Representative flow cytometric analysis images of cell apoptosis after different treatments as indicated.

(B) Western blotting images showing the expression of c-caspase3 in 4T1 cells after different treatments as indicated. The raw data are shown in Figure S31.

(C and D) Schematic illustrating the design of animal experiments in 4T1 tumor-bearing mice (C) and average tumor growth curves of 4T1 tumors in mice with various treatments as indicated (D). Data are presented as the mean ± SEM (n = 6).

(E) Average tumor growth curves of MDA-MB-231 tumors in mice with various treatments as indicated. Data are presented as the mean ± SEM (n = 6).

(F) Western blotting images showing the expression of LC3 I and LC3 II in 4T1 cells after culture with different concentrations of *F. nucleatum* for 24 h. The raw data are shown in Figure S32.

(G) Autophagosomes were observed by TEM in 4T1 cells with or without *F. nucleatum* infection. Scale bars, 5 μm.

Figure 3. *Continued*

(H) Relative viabilities of 4T1 cells infected with *F. nucleatum* after different treatments with different concentrations of 5Fu with or without CQ.

(I) Volcano plot for the transcriptome sequencing of 4T1 cells with or without *F. nucleatum* infection.

(J) GO enrichment analysis of the differential pathways treated to *F. nucleatum* infection. Statistical significance was calculated via two-tailed Student's t test (D and E) in GraphPad Prism. *p < 0.05; **p < 0.01; ***p < 0.001; ****p < 0.0001.

Figures 3H and S13, *F. nucleatum*-induced chemoresistance in 4T1 cells was abolished after the addition of the autophagy lysosomal inhibitor CQ, whereas CQ itself induced negligible effect on 4T1 cells. These findings collectively indicated that *F. nucleatum* activated the autophagy pathway in breast cancer cells and contributed to the development of chemoresistance.

In addition to autophagy, epithelial-mesenchymal transition (EMT) of cancer cells may be closely related to chemoresistance.[31] As shown in Figure S14, with the increase of *F. nucleatum* levels, the content of E-cadherin decreased while the content of N-cadherin increased, indicating that *F. nucleatum* indeed could induce the chemotherapy resistance via EMT. Besides, we further investigated the uptake of chemotherapeutic drugs of cancer cells with or without *F. nucleatum* infection. As shown in Figure S15, *F. nucleatum* induced nearly no effect on the uptake of chemotherapeutic drugs by breast cancer cells. In delving deeper into the underlying mechanisms associated with the chemoresistance induced by *F. nucleatum*, the RNA-sequencing of 4T1 cells with or without *F. nucleatum* infection was carried out. A comprehensive analysis unveiled 110 differentially expressed genes, comprising 60 upregulated genes and 50 downregulated genes (Figure 3I). Through Gene Ontology (GO) analysis of biological processes, our exploration revealed that following *F. nucleatum* infection, a majority of differentially expressed genes were found to be enriched in the interleukin-1-related pathway—a pathway recognized for its role in promoting tumor growth and metastasis (Figure 3J).[32] Consistent with the results of RNA-sequencing, 4T1 cells incubated with *F. nucleatum* exhibited increased secretion of interleukin-1β (IL-1β) (Figure S16).

Preparation and characterization of LipoFM with tumor-targeting ability

Considering the role of tumor-colonizing *F. nucleatum* in inducing chemoresistance in breast cancer, we further investigated whether eliminating those tumor-colonizing bacteria would be beneficial to overcome chemoresistance. Utilizing antibiotics to eradicate pathogenic bacteria remains the most commonly used strategy.[33] However, a high dosage and frequent dosing regimen are usually needed to eliminate tumor-resident bacteria, which may inadvertently cause damage to the gut and other tumor microbiota and even contribute to the emergence of multidrug-resistant strains.[24,34] Therefore, it is imperative to develop a targeted delivery system capable of effectively delivering antibiotics to bacteria-colonizing tumors and enabling the selective eradication of microbes within tumors. Given the high affinity between the membrane protein Fap-2 of *F. nucleatum* and Gal-GalNAc expressed in breast tumors, leveraging the membrane of *F. nucleatum* may be a type of targeted delivery carrier for breast tumors colonized with *F. nucleatum*.

First, the cytoplasmic membrane of *F. nucleatum* containing Fap-2 was isolated from the lysate of *F. nucleatum* after density gradient centrifugation, and the presence of various cytoplasmic proteins in FM was confirmed by sodium dodecyl sulfate-polyacrylamide gel electrophoresis (SDS-PAGE). As depicted in Figure 4A, although a reduced quantity of proteins was found in FM, the content of Fap-2 protein remained nearly unchanged. Meanwhile, liquid chromatography with tandem mass spectrometry (LC-MS/MS) was used for quantitative analysis of different proteins

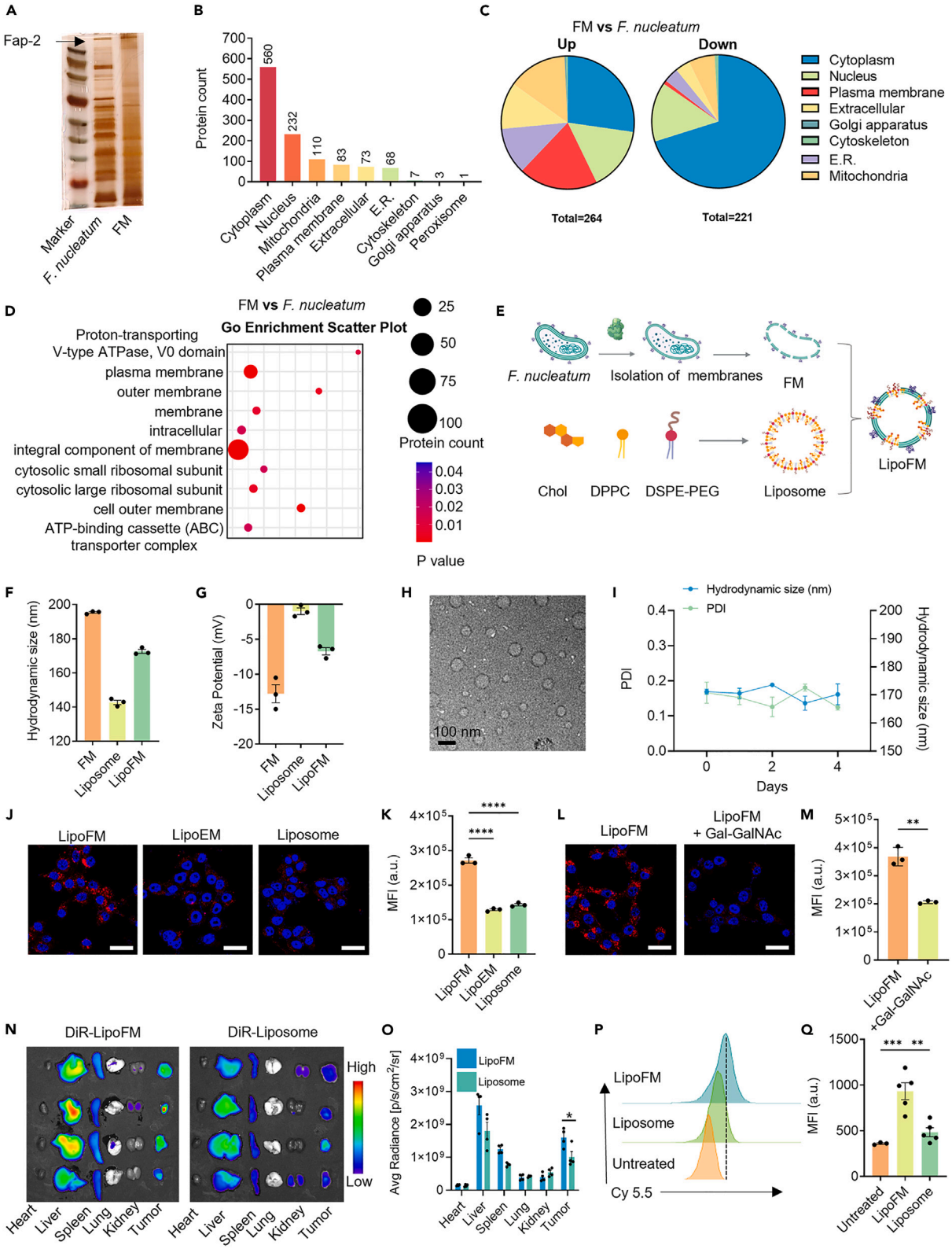
A
Fap-2
Marker
F. nucleatum
FM
B
Protein count
700
600
500
400
300
200
100
0
560
232
110
83
73
68
7
3
1
Cytoplasm
Nucleus
Mitochondria
Plasma membrane
Extracellular
E.R.
Cytoskeleton
Golgi apparatus
Peroxisome
C
FM vs F. nucleatum
Up
Down
Total=264
Total=221
Cytoplasm
Nucleus
Plasma membrane
Extracellular
Golgi apparatus
Cytoskeleton
E.R.
Mitochondria
D
FM vs F. nucleatum
Go Enrichment Scatter Plot
Proton-transporting V-type ATPase, V0 domain
plasma membrane
outer membrane
membrane
intracellular
integral component of membrane
cytosolic small ribosomal subunit
cytosolic large ribosomal subunit
cell outer membrane
ATP-binding cassette (ABC) transporter complex
25
50
75
100
Protein count
0.04
0.03
0.02
0.01
P value
E
F. nucleatum
Isolation of membranes
FM
Chol
DPPC
DSPE-PEG
Liposome
LipoFM
F
Hydrodynamic size (nm)
200
180
160
140
120
FM
Liposome
LipoFM
G
Zeta Potential (mV)
0
-5
-10
-15
-20
FM
Liposome
LipoFM
H
100 nm
I
Hydrodynamic size (nm)
PDI
0.4
0.3
0.2
0.1
0.0
200
190
180
170
160
150
0
2
4
Days
J
LipoFM
LipoEM
Liposome
K
MFI (a.u.)
4×10^5
3×10^5
2×10^5
1×10^5
0
****
****
LipoFM
LipoEM
Liposome
L
LipoFM
LipoFM + Gal-GalNAc
M
MFI (a.u.)
5×10^5
4×10^5
3×10^5
2×10^5
1×10^5
0
**
LipoFM
+Gal-GalNAc
N
DiR-LipoFM
DiR-Liposome
High
Low
Heart
Liver
Spleen
Lung
Kidney
Tumor
O
Avg Radiance [p/s/cm²/sr]
4×10^9
3×10^9
2×10^9
1×10^9
0
LipoFM
Liposome
*
Heart
Liver
Spleen
Lung
Kidney
Tumor
P
LipoFM
Liposome
Untreated
Cy 5.5
Q
MFI (a.u.)
1500
1000
500
0
*** **
Untreated
LipoFM
Liposome

Figure 4. The targeting ability of LipoFM to Gal-GalNAc-overexpressing breast tumors

(A) SDS–PAGE pattern of proteins from whole *F. nucleatum* lysate and FM.

(B) Subcellular location annotation of the total proteins identified in both FM and *F. nucleatum*.

(C) The distribution of differential proteins of FM versus *F. nucleatum*.

(D) GO enrichment analysis of the upregulated cellular component in FM versus *F. nucleatum*.

(E) Schematic illustrating the preparation of LipoFM.

(F and G) The hydrodynamic sizes (F) and zeta potentials (G) of liposome, FM, and LipoFM. Data are presented as the mean ± SEM (n = 3).

(H) TEM image of LipoFM (scale bars, 100 nm).

(I) Time-lapse hydrodynamic size and PDI of LipoFM. Data are presented as the mean ± SEM (n = 3).

(J and L) Confocal microscopy images of 4T1 cells incubated with LipoFM, LipoEM, and liposome (J) or LipoFM and LipoFM + Gal-GalNAc (L) for 24 h, in which LipoFM, LipoEM, and liposome were labeled with DiD (red) and cell nuclei were labeled with DAPI (blue). Scale bars, 20 μm.

(K and M) Statistical analysis of flow cytometry of DiD intensity in 4T1 cells after incubation with DiD-LipoFM, DiD-LipoEM, and DiD-liposome (K) or DiD-LipoFM and DiD-LipoFM + Gal-GalNAc (M) for 24 h. Data are presented as the mean ± SEM (n = 3).

(N) *Ex vivo* DiR fluorescence images of the main organs and tumors collected from mice with different treatments as indicated at 72 h post injection.

(O) Statistical analysis of average DiR fluorescence signals in main organs and tumors based on the images in (N). Data are presented as the mean ± SEM (n = 4).

(P and Q) Representative flow cytometric analysis plots (P) and statistical analysis (Q) of the intensity of Cy5.5 in tumors collected from mice after different treatments at 72 h post injection. Data are presented as the mean ± SEM (n = 3 for untreated group and n = 5 for liposome and LipoFM treated group). Statistical significance was calculated via one-way ANOVA (K and Q) or two-tailed Student's t test (M and O) in GraphPad Prism. *$p < 0.05$; **$p < 0.01$; ***$p < 0.001$; ****$p < 0.0001$.

in FM and *F. nucleatum*. As shown in Figures 4B and 4C, among the 1,137 identified proteins, numerous plasma membrane proteins were upregulated in FM, whereas a variety of cytoplasmic proteins were downregulated in comparison with *F. nucleatum*. GO analysis also revealed that the upregulated proteins in FM were enriched in the plasma membrane, outer membrane, membrane, and integral component of the membrane, indicating successful extraction of the *F. nucleatum* membrane (Figure 4D). Next, the FM was extruded through the 200 nm polycarbonate hydrophilic membrane filter to obtain FM nanovehicles. Although FM vesicles were successfully obtained, the hydrodynamic size and polydispersity index (PDI) of FM vesicles increased obviously over time (Figure S17), which may be contributed to the aggregation of natural membrane.[35]

To stabilize the obtained FM, we fused it with a liposome that was synthesized by reverse-phase evaporation using the typical formulation.[35–37] Specifically, the FM and liposome were repeatedly extruded through the extruder to generate liposomes containing FM (LipoFM) (Figure 4E). To verify the successful fusion of FM and liposome, FM labeled with tetramethylrhodamine B (TRITC) was fused with liposome labeled with FITC by repeated physical extrusions. After extrusion, the fluorescence from FITC decreased, whereas the fluorescence from TRITC increased due to Forster resonance energy transfer, indicating the successful fusion of FM and liposome (Figure S18). The hydrodynamic diameter and surface zeta potential of LipoFM were measured to be approximately 170 nm and −7 mV, respectively (Figures 4F and 4G). Both the hydrodynamic diameter and surface zeta potential of LipoFM were intermediate between those of liposome and FM, further confirming the successful fusion of FM and liposome. As depicted in Figure 4H, LipoFM exhibited a uniform distribution and spherical morphology in the TEM image. Moreover, the hydrodynamic sizes and PDI of LipoFM remained nearly unchanged over 4 days, indicating the significantly enhanced stability of FM after fusion with liposome (Figure 4I).

Motivated by the specific binding of *F. nucleatum* to Gal-GalNAc, we conducted the investigation to determine whether LipoFM had the capacity to target and attach to Gal-GalNAc overexpressed breast cancer cells (Figure S19). In this study, 4T1 cells were incubated with 1,1′-Dioctadecyl-3,3,3′,3′-Tetramethylindodicarbocyanine,4-Chlorobenzenesulfonate Salt (DiD) labeled LipoFM (DiD-LipoFM), DiD-LipoEM

(formed from liposomes and the *E. coli* cytoplasmic membrane), and DiD-liposome. 24 h later, 4T1 cells were collected for confocal imaging and flow cytometry analysis. As exhibited in Figures 4J and 4K, the mean fluorescence intensity of 4T1 cells incubated with LipoFM was significantly higher than that of cells incubated with LipoEM or liposome. To confirm the Fap-2-Gal-GalNAc-mediated targeting and binding of LipoFM to 4T1 cells, cells were incubated with Gal-GalNAc-pretreated LipoFM. As indicated in Figures 4L and 4M, LipoFM after pre-incubation with Gal-GalNAc exhibited significantly reduced adhesion capacity to 4T1 cells. By contrast, the addition of Gal-GalNAc induced negligible effects on the binding of LipoFM to melanoma B16F10 cells with low Gal-GalNAc expression (Figure S20).

Encouraged by the successful targeting and binding of LipoFM to breast cancer cells, we proceeded to investigate its targeting ability *in vivo*. Mice bearing subcutaneous 4T1 tumors were i.v. injected with 1,1′-dioctadecyl-3,3,3′,3′-tetramethylindotricarbocyanine iodide (DiR)-labeled LipoFM (DiR-LipoFM) and DiR-liposome. Compared with the DiR-liposome group, mice injected with DiR-LipoFM exhibited a significantly enhanced fluorescence signal in tumors (Figure S21). 72 h later, the mice were sacrificed, and their tumors and other major organs were collected for fluorescence imaging. It was found that the fluorescence intensity from DiR in tumors collected from mice injected with DiR-LipoFM was approximately 1.5 times higher than that in tumors collected from mice injected with DiR-liposome (Figures 4N and 4O), and slightly increased liver accumulation of LipoFM was also observed, which might be attributed to the high expression of Gal-GalNAc in the liver (Figure S22). We also analyzed the targeting and binding ability of LipoFM in tumors after injection with Cyanine 5.5 (Cy5.5)-labeled LipoFM (Cy5.5-LipoFM) and Cy5.5-liposome using flow cytometry. Consistent with the improved tumor retention capacity, LipoFM exhibited obviously increased cellular uptake within tumors (Figures 4P and 4Q). Moreover, LipoFM showed nearly no toxicity to major organs of mice (Figure S23).

Tumor-targeted delivery of antibiotics using LipoFM

Encouraged by the targeted delivery ability of LipoFM, we further investigated the potential of LipoFM as a delivery carrier for antibiotics to *F. nucleatum*-infected tumors. Colistin, an effective antibiotic that has been widely used for drug-resistant Gram-negative bacteria, was chosen in our work.[38] First, colistin was encapsulated in liposome using the emulsion solvent evaporation method and then fused with FM as described above.[39] The loading efficiencies of colistin in liposome and LipoFM were measured to be ~17% and 14%, respectively. Then, the release profiles of colistin from Colistin-LipoFM were evaluated via high-performance liquid chromatography (HPLC). Notably, Colistin-LipoFM displayed a sustained release profile of colistin in both phosphate-buffered saline (PBS) and cell culture media, as demonstrated in Figure S24.

To explore the targeted uptake of Colistin-LipoFM in 4T1 cells, cells after incubation with free colistin, Colistin-Liposome, and Colistin-LipoFM with the same colistin dosage of 100 μg/mL for 24 h were collected for HPLC analysis. As shown in Figure 5A, significantly higher amounts of colistin could be detected in cells incubated with Colistin-LipoFM, whereas the PEGylated liposome decreased the overall endocytosis efficiency of colistin.[40] Furthermore, mice bearing 4T1 tumors were i.v. injected with free colistin, Colistin-Liposome, or Colistin-LipoFM to quantitatively measure the targeted drug delivery of Colistin-LipoFM *in vivo*. 24 h after injection, the tumors and major organs were homogenized and extracted for HPLC analysis. As shown in Figure 5B, despite delayed Colistin-Liposome internalization *in vitro*, the tumors collected from mice injected with Colistin-Liposome showed higher

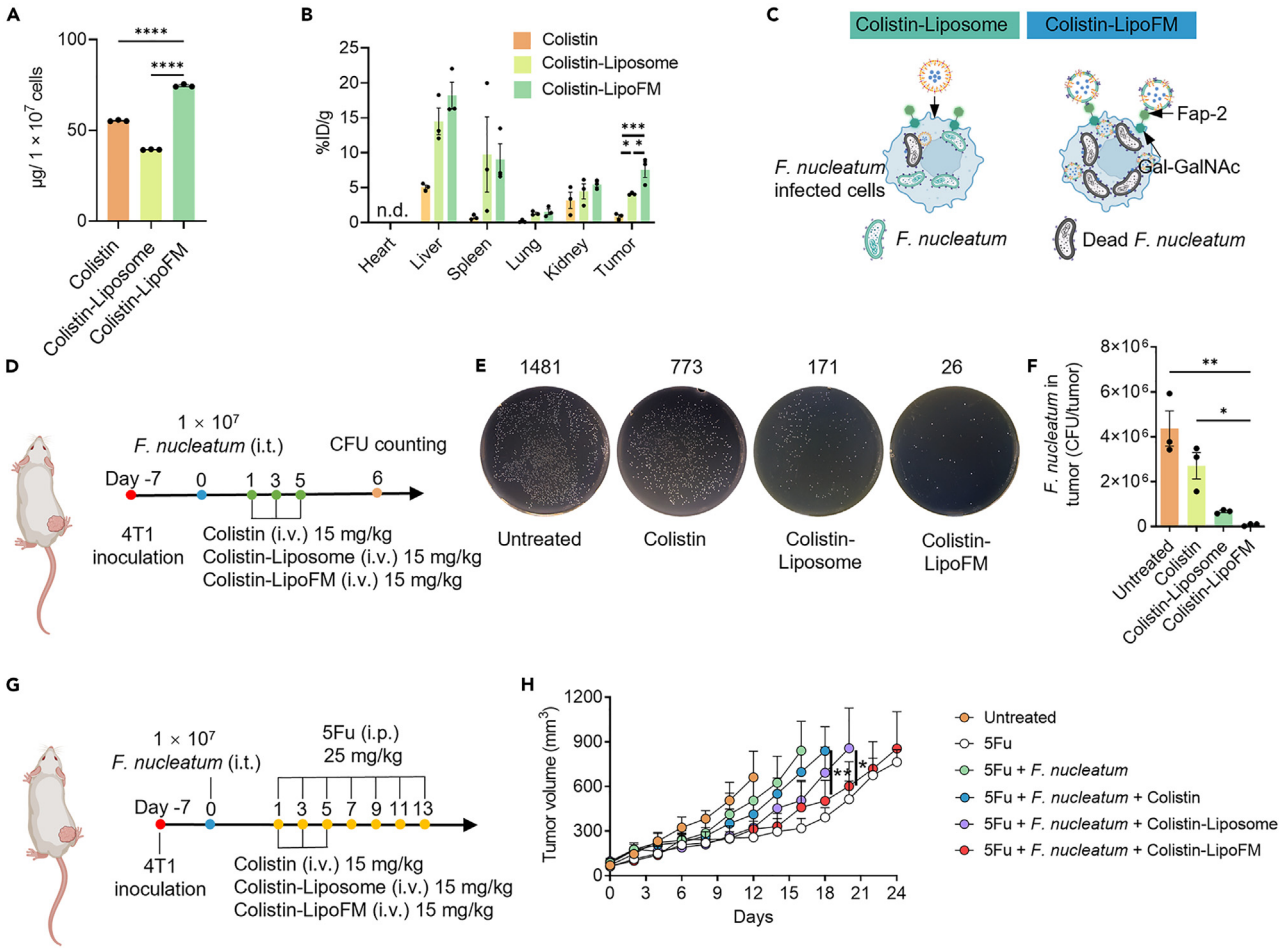

Figure 5. Colistin-LipoFM for depletion of tumor-colonizing *F. nucleatum*

(A) The concentration of colistin in 4T1 cells after co-cultured with different formulations. Data are presented as the mean ± SEM (n = 3).

(B) Biodistribution of free colistin, Colistin-Liposome, and Colistin-LipoFM in mice bearing 4T1 tumors at 24 h post injection by recording the concentration of colistin using HPLC. Data are presented as the mean ± SEM (n = 3).

(C) Schematic showing Colistin-LipoFM to selectively eliminate tumor-colonized bacteria.

(D) Scheme showing the experimental schedule in mice bearing 4T1 tumors.

(E and F) Colony plate images (E) and statistical analysis of the CFUs (F) showing the abundance of *F. nucleatum* in homogenized tumors of mice with different treatments as indicated. The black number in each picture indicates the number of CFUs in each plate. The dilution of homogenized tumor solutions was 20,000. Data are presented as the mean ± SEM (n = 3).

(G) Scheme showing the experimental schedule in mice bearing 4T1 tumors.

(H) Average tumor growth curves of 4T1 tumors in mice with various treatments as indicated. Growth curves were stopped when the tumor volumes were larger than 1,000 mm^3 in the corresponding group. Data are presented as the mean ± SEM (n = 8). Statistical significance was calculated via one-way ANOVA (A,B, and F) or two-tailed Student's t test (H) in GraphPad Prism. *p < 0.05; **p < 0.01; ***p < 0.001; ****p < 0.0001.

concentrations of colistin than free colistin. However, the tumors collected from mice injected with Colistin-LipoFM showed the highest concentration of colistin. Thus, the specific binding between LipoFM and cancer cells could remarkably promote the uptake of colistin in tumors.

Encouraged by the specific binding between LipoFM and cancer cells *in vitro* and *in vivo*, we proceeded to investigate the intracellular and intratumoral *F. nucleatum* killing efficiency using colistin in different formulations (Figure 5C). First, *F. nucleatum*-infected 4T1 cells were co-cultured with free colistin, Colistin-LipoFM, and Colistin-Liposome with the same colistin concentration of 5 μM (6.76 μg/mL).

24 h later, the cells were washed and lysed for colony counting. As shown in Figures S25A and S25B, cells incubated with Colistin-LipoFM exhibited the lowest level of *F. nucleatum*. Although the cells incubated with free colistin exhibited a reduced level of *F. nucleatum*, it was still non-negligible. By contrast, compared with the untreated group, Colistin-Liposome exhibited nearly no killing effect on intracellular infected *F. nucleatum*, and the reduction in cytotoxicity of Colistin-Liposome may be attributed to the delayed cellular uptake *in vitro*.

Inspired by the excellent intracellular *F. nucleatum* killing effect, we further investigated the killing effect of Colistin-LipoFM on tumor-resident *F. nucleatum* in 4T1 tumor models. As shown in Figure 5D, 7 days after inoculating the 4T1 tumors, 1×10^7 CFU of *F. nucleatum* was i.t. injected, and then free colistin, Colistin-Liposome, and Colistin-LipoFM were i.v. administered with the same colistin dosage of 15 mg/kg on days 1, 3, and 5. On day 6, the mice were sacrificed, and their tumors were collected for CFU determination. Excitingly, the CFU of *F. nucleatum* collected from mice treated with Colistin-LipoFM was significantly reduced (Figures 5E and 5F). Colistin-Liposome exhibited an enhanced killing effect compared with that treated with free colistin, but its *F. nucleatum* killing efficacy was still much lower than that achieved by Colistin-LipoFM, demonstrating that Colistin-LipoFM exhibited the most effective ability to inhibit *F. nucleatum* proliferation in tumors due to the specific binding between LipoFM and cancer cells.

After successfully eliminating tumor-colonizing *F. nucleatum* with Colistin-LipoFM, we sought to investigate whether this treatment could alleviate *F. nucleatum*-induced chemoresistance in breast tumors. Thus, mice bearing 4T1 breast tumors were randomly allocated into six groups: (1) Untreated, (2) 5Fu intraperitoneal injection (i.p.), (3) 5Fu (i.p.) + *F. nucleatum* (i.t.), (4) 5Fu (i.p.) + *F. nucleatum* (i.t.) + free colistin (i.v.), (5) 5Fu (i.p.) + *F. nucleatum* (i.t.) + Colistin-Liposome (i.v.), and (6) 5Fu (i.p.) + *F. nucleatum* (i.t.) + Colistin-LipoFM (i.v.). *F. nucleatum* was i.t. administered at the dose of 1×10^7 CFU per tumor on day 0, 5Fu was i.p. injected at the dose of 25 mg/kg on days 1, 3, 5, 7, 9, 11, and 13, and free colistin, Colistin-Liposome, and Colistin-LipoFM was i.v. injected with the colistin dose of 15 mg/kg on days 1, 3, and 5 (Figure 5G). The tumor size was measured every 2 days. As shown in Figures 5H and S26, the tumors in the 5Fu (i.p.) + *F. nucleatum* (i.t.) + Colistin-LipoFM (i.v.) group displayed similar growth curves to those in the 5Fu (i.p.) group without *F. nucleatum* infection, indicating that Colistin-LipoFM could successfully eliminate *F. nucleatum* and alleviate *F. nucleatum*-induced chemoresistance. By contrast, Colistin-Liposome could slightly delay the growth of tumors with *F. nucleatum* infection due to their limited accumulation in tumors. In addition, free colistin exhibited nearly no effect to chemotherapeutic effect in tumors with *F. nucleatum* infection due to its limited elimination of *F. nucleatum*. Therefore, Colistin-LipoFM was able to successfully reverse *F. nucleatum*-induced chemoresistance, improving the therapeutic efficiency of chemotherapy in *F. nucleatum*-infected breast cancer tumors.

LipoFM as a targeted drug delivery platform to inhibit lung metastases

In addition to *F. nucleatum*, it has been reported that some tumor-colonizing bacteria, including *Streptococcus*, *Staphylococcus*, and *Lactobacillus*, could promote the survival of cancer cells against fluid shear stress during circulation to accelerate cancer metastasis.[24] Consistent with published work, the abovementioned bacteria have also been detected in human breast tumors in our clinical cohort (Figure S27). Encouraged by the successful elimination of tumor-colonizing *F. nucleatum* by Colistin-LipoFM, we then explored whether LipoFM could act as a targeted delivery carrier of antibiotics to eliminate other bacteria in breast tumors to prevent cancer

metastasis. First, various antibiotics, including colistin, vancomycin hydrochloride, and Doxy, were co-cultured with *F. nucleatum*, *Streptococcus sanguis* (*S. sanguis*), *Staphylococcus xylosus* (*S. xylosus*), or *Enterococcus faecalis* (*E. faecalis*), which are common tumor-resident bacteria, to screen the antibiotic. As shown in Figures 6A and S28, among all the detected antibiotics, Doxy exhibited the most effective inhibitory effect on all these bacteria. Thus, Doxy was chosen for encapsulation into LipoFM with the loading efficiency and loading capacity of ~ 17% and ~ 6%, respectively. Moreover, Doxy-LipoFM exhibited a sustained release profile of Doxy in PBS and cell culture media (Figure 6B).

Next, the intracellular delivery efficiency of Doxy-LipoFM was investigated. 4T1 cells were incubated with free Doxy, Doxy-Liposome, and Doxy-LipoFM with similar Doxy concentrations of 100 μg/mL for 24 h, and the intracellular Doxy concentration was quantified by HPLC. As expected, the level of Doxy in cells incubated with Doxy-LipoFM was significantly higher than that in cells incubated with free Doxy and Doxy-Liposome (Figure S29). Then, the tumor accumulation of Doxy was investigated in mice bearing 4T1 tumors. Mice bearing 4T1 tumors were i.v. administered with free Doxy, Doxy-Liposome, and Doxy-LipoFM with similar Doxy dose at 15 mg/kg, and the mice were sacrificed, and their tumors were collected to analyze the concentration of Doxy 24 h later. It was found that the tumors collected from mice administered with Doxy-LipoFM also exhibited markedly enhanced intratumoral concentrations of Doxy (Figure 6C).

Inspired by the effective intratumoral delivery of antibiotics achieved by LipoFM, we next examined the potential of Doxy-LipoFM in eliminating intratumoral bacteria. To simulate clinical conditions that tumors with variety of bacteria, BALB/c mice bearing 4T1 cells were i.t. injected with a mixture of *F. nucleatum* (2×10^6 CFU), *S. sanguis* (2×10^6 CFU), *S. xylosus* (2×10^6 CFU), and *E. faecalis* (2×10^6 CFU) on day 0, and then the tumors were collected for CFU counting on days 1, 3, 6, 10, and 14. Abundant bacteria were observed even on day 14, indicating the successful colonization of bacteria in 4T1 tumors (Figure S30). Then free Doxy, Doxy-Liposome, and Doxy-LipoFM were i.v. administered with a similar Doxy dosage of 15 mg/kg. On day 6, the tumors were collected for CFU determination (Figure 6D). Similar to the above results, compared with the untreated group, free Doxy exhibited a slight impact on the growth of bacteria in the tumor. Although the growth of intratumoral bacteria was inhibited in mice treated with Doxy-Liposome, the level of intratumoral bacteria was still non-negligible. By contrast, the CFU of bacteria in mice treated with Doxy-LipoFM was significantly reduced, demonstrating that antibiotic-loaded LipoFM could indeed effectively eliminate tumor-colonizing bacteria (Figures 6E and 6F).

Having confirmed the effective antibacterial ability of Doxy-LipoFM, we further investigated whether Doxy-LipoFM could eliminate microbiota in breast tumors to prevent cancer metastasis. Specifically, highly tumorigenic and invasive luciferase-transfected 4T1 cells (4T1-luc) were injected into the breast pads of BALB/c mice to establish an orthotopic breast tumor model on day −7, and *F. nucleatum* (2×10^6 CFU), *S. sanguis* (2×10^6 CFU), *S. xylosus* (2×10^6 CFU), and *E. faecalis* (2×10^6 CFU) were i.t. injected into the breast tumor on day 0. Then, Doxy-LipoFM was i.v. injected with the Doxy dose of 15 mg/kg on days 1, 3, and 5 (Figure 6G), and the mice were imaged by an *in vivo* imaging system (IVIS) to track the metastasis of cancer cells. Consistent with previous literature, mice with bacterial infection exhibited remarkably improved bioluminescence signals from cancer cells in the lung, indicating that bacterial infection could indeed promote cancer metastasis.[24,27] Interestingly, mice with bacterial infection after Doxy-LipoFM treatment exhibited

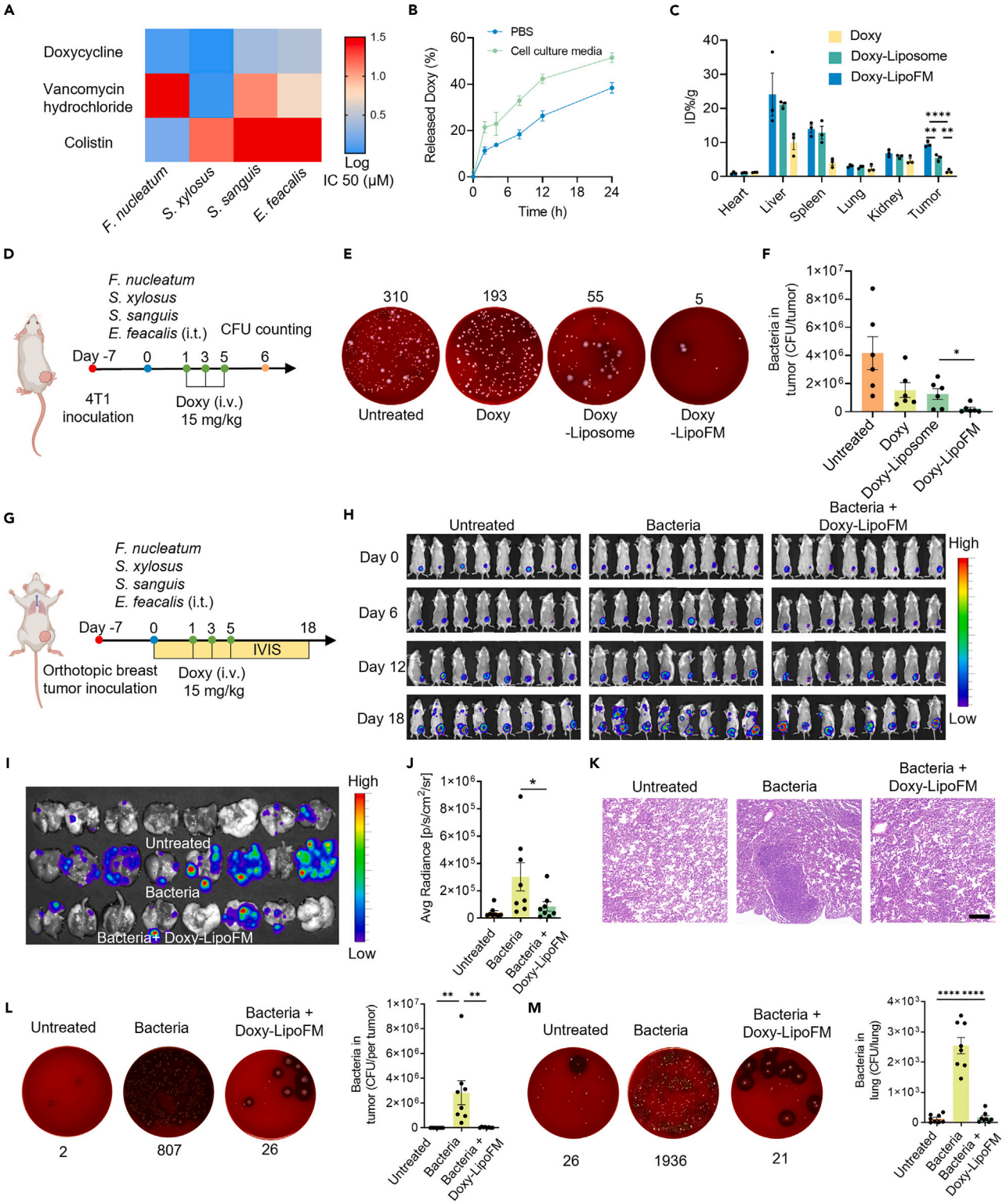

Figure 6. Doxy-LipoFM for depletion of tumor-colonizing bacteria

(A) Heatmap showing the IC 50 of Doxy, vancomycin hydrochloride, and colistin to different bacteria.

(B) The release profiles of Doxy from Doxy-LipoFM incubated in PBS or cell culture media. Data are presented as the mean ± SEM (n = 3).

Figure 6. *Continued*

(C) Biodistribution of free Doxy, Doxy-Liposome, and Doxy-LipoFM in mice bearing 4T1 tumors at 24 h post injection by recording the concentration of Doxy using HPLC. Data are presented as the mean ± SEM (n = 3).

(D) Scheme showing the experimental schedule in mice bearing 4T1 tumors.

(E and F) Colony plate images (E) and the statistical analysis of CFUs (F) showing the bacterial abundance in homogenized tumors of mice with different treatments as indicated. The black number in each picture indicates the number of CFUs in each plate. The dilution of these homogenized solutions was 20,000. Data are presented as the mean ± SEM (n = 6).

(G) Scheme and timeline showing the experimental design to evaluate the therapeutic efficacies of Doxy-LipoFM to inhibit bacteria-induced lung metastases.

(H) *In vivo* bioluminescence images to track the metastases of luciferase-transferred 4T1 cancer cells.

(I and J) *Ex vivo* bioluminescence images (I) and corresponding statistical data (J) of lungs collected from mice with different treatments. Data are presented as the mean ± SEM (n = 8).

(K) H&E staining images of lungs showing metastasis in the lungs of mice after different treatments.

(L and M) Colony plate images (left) and statistical data of CFUs (right) showing the bacterial abundance in homogenized tumors (L) and lungs (M) of mice with different treatments. The black number in each picture indicates the number of CFUs in each plate. Data are presented as the mean ± SEM (n = 8). Statistical significance was calculated via one-way ANOVA (C, J, L, and M) or via two-tailed Student's t test (F) in GraphPad Prism. *$p < 0.05$; **$p < 0.01$; ***$p < 0.001$; ****$p < 0.0001$.

a reduced bioluminescence signal, which was similar to that in mice without bacterial infection (Figure 6H). To further investigate the impact of Doxy-LipoFM on cancer metastasis, the mice were sacrificed, and their lungs were collected for different analyses. *Ex vivo* bioluminescence imaging further demonstrated that Doxy-LipoFM could inhibit the cancer metastasis induced by infected bacteria (Figures 6I and 6J). As shown in the H&E staining images of lungs collected from mice with different treatments, significantly increased tumor metastasis was observed in the lungs in the bacteria-infected groups, whereas Doxy-LipoFM treatment resulted in a strong reduction in lung metastasis. Meanwhile, orthotopic and lung metastatic tumors were collected for CFU determination. As expected, both the orthotopic tumors and lung metastatic tumors exhibited significantly reduced bacterial burden after Doxy-LipoFM treatment (Figures 6L and 6M). All these results demonstrated that our proposed Doxy-LipoFM could successfully reduce the pulmonary metastases of breast cancer with bacterial infection.

Doxy-LipoFM promotes combined chemotherapy for orthotopic breast cancer

Combination chemotherapy using cyclophosphamide (CTX), methotrexate (MTX), and 5Fu (CMF) regimen is the first line of clinical treatment for patients with breast cancer.[41,42] As tumor-resident bacteria play an important role in promoting tumor metastasis and reducing responses to chemotherapy, it is important to investigate whether Doxy-LipoFM could promote combination chemotherapy for breast cancer with bacterial infection. Thus, the mice bearing orthotopic breast tumors were randomly divided into five groups: (1) untreated, (2) bacteria (i.t.), (3) CMF (i.p.), (4) CMF (i.p.) + bacteria, and (5) CMF (i.p.) + bacteria (i.t.) + Doxy-LipoFM (i.v.). Models with various bacterial infection were established as mentioned above, CTX and, MTX were i.p. injected with doses of 100 mg/kg and 20 mg/kg on days 1 and 7, and 5Fu was i.p. injected at the dose of 25 mg/kg on days 1, 3, 5, 7, 9, 11, and 13. Then, Doxy-LipoFM was i.v. injected with the Doxy dose of 15 mg/kg on days 1, 3, and 5. The size of primary tumors was measured every 2 days (Figure 7A). As shown in Figures 7B and 7C, bacterial infection exhibited a negligible effect on the growth of primary tumors but obviously reduced the therapeutic effect of CMF. The tumors in the CMF + Bacteria + Doxy-LipoFM group displayed similar growth curves to those in the CMF group without bacterial infection, even leading to complete regression of established tumors in two mice. In addition to the tumor growth curves, 18 days after different treatments, mice were euthanized, and their tumors were collected for different analyses. The tumor weights in different groups further indicated that the therapeutic results of CMF could be successfully recovered with the help of

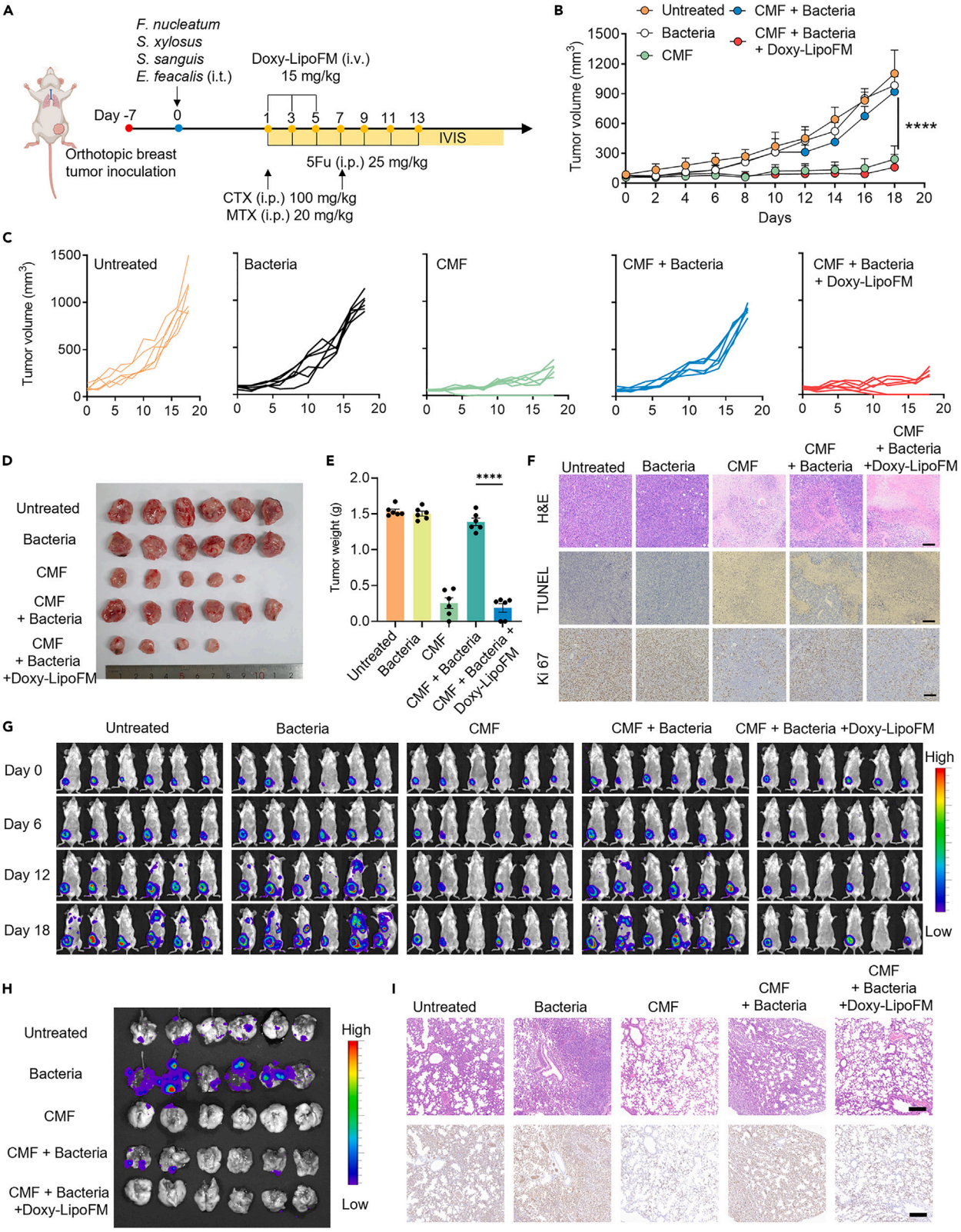
A
F. nucleatum
S. xylosus
S. sanguis
E. feacalis (i.t.)
Doxy-LipoFM (i.v.)
15 mg/kg
Day -7
0
1 3 5 7 9 11 13
IVIS
Orthotopic breast
tumor inoculation
5Fu (i.p.) 25 mg/kg
CTX (i.p.) 100 mg/kg
MTX (i.p.) 20 mg/kg
B
Untreated
Bacteria
CMF
CMF + Bacteria
CMF + Bacteria
+ Doxy-LipoFM
Tumor volume (mm3)
Days
****
C
Untreated
Bacteria
CMF
CMF + Bacteria
CMF + Bacteria
+ Doxy-LipoFM
Tumor volume (mm3)
D
Untreated
Bacteria
CMF
CMF
+ Bacteria
CMF
+ Bacteria
+Doxy-LipoFM
E
Tumor weight (g)
****
Untreated
Bacteria
CMF
CMF + Bacteria
CMF + Bacteria +
Doxy-LipoFM
F
Untreated
Bacteria
CMF
CMF
+ Bacteria
CMF
+ Bacteria
+Doxy-LipoFM
H&E
TUNEL
Ki 67
G
Untreated
Bacteria
CMF
CMF + Bacteria
CMF + Bacteria +Doxy-LipoFM
Day 0
Day 6
Day 12
Day 18
High
Low
H
Untreated
Bacteria
CMF
CMF + Bacteria
CMF + Bacteria
+Doxy-LipoFM
High
Low
I
Untreated
Bacteria
CMF
CMF
+ Bacteria
CMF
+ Bacteria
+Doxy-LipoFM

Figure 7. Doxy-LipoFM promotes the therapeutic effect of combination chemotherapy in an orthotopic breast tumor model

(A) Scheme and timeline showing the experimental design to evaluate the therapeutic efficacies of Doxy-LipoFM to promote the therapeutic effect of combination chemotherapy in a bacteria-infected orthotopic breast tumor model.

(B and C) Average (B) and individual (C) tumor growth curves of the primary 4T1 tumors in mice with various treatments as indicated. Data are presented as the mean ± SEM (n = 6).

(D and E) Images (D) and weights (E) of primary 4T1 tumors harvested from mice after different treatments. Data are presented as the mean ± SEM (n = 6).

(F) H&E, TUNEL, and Ki67 staining of tumor slices collected from mice 18 days after different treatments as indicated.

(G) *In vivo* bioluminescence images to track the metastases of luciferase-transferred 4T1 cancer cells after different treatments as indicated.

(H) *Ex vivo* bioluminescence images of lungs collected from mice with different treatments.

(I) H&E and Ki67 staining images of lungs showing lung metastasis in mice after different treatments. Statistical significance was calculated via two-way ANOVA (B) or via one-way ANOVA (E) in GraphPad Prism. *$p < 0.05$; **$p < 0.01$; ***$p < 0.001$; ****$p < 0.0001$.

Doxy-LipoFM in bacteria-infected tumors. To completely assess the influence of tumor-resident bacteria on the CMF regimen and the therapeutic effect of Doxy-LipoFM, the tumors were collected for histological analysis. The H&E and TUNEL staining images visually revealed that tumors collected from the CMF without bacterial infection and CMF + Bacteria + Doxy-LipoFM groups exhibited the most severe damage/cell apoptosis, whereas tumors collected from the CMF + Bacteria group showed moderate cell damage/apoptosis, which was comparable to those in untreated group (Figure 7F). Meanwhile, the tumor slides in both CMF and CMF + Bacteria + Doxy-LipoFM exhibited an obviously dimmed Ki67 signal, an important marker of cell proliferation, further indicating the synergistic chemotherapy achieved by combining CMF with Doxy-LipoFM in bacteria-infected tumors.

Additionally, the progression of cancer metastases was monitored by IVIS according to the bioluminescence signal from 4T1-luc. As shown in Figure 7G, mice with bacterial infections exhibited a remarkable increase in the bioluminescence signal from cancer cells in the lung. Although CMF treatment slightly reduced cancer metastasis in bacteria-infected mice, cancer lung metastasis was still obvious. Excitingly, the combination of CMF and Doxy-LipoFM successfully inhibited cancer metastasis. To further investigate the therapeutic effect of Doxy-LipoFM and CMF, the mice were also sacrificed, and their lungs were collected for different analyses. *Ex vivo* bioluminescence imaging further demonstrated that Doxy-LipoFM indeed improved the therapeutic responses of CMF to bacteria-induced lung metastasis (Figure 7H), which was further demonstrated in the H&E and Ki67 staining images (Figure 7I). All these results demonstrate that our proposed Doxy-LipoFM should be a promising adjunct for combination chemotherapy in treating breast cancer.

DISCUSSION

In this study, we analyzed the microbes in clinical samples and found the widespread existence of *F. nucleatum* colonization in human breast tumors, as mediated by the interactions between membrane protein Fap-2 in *F. nucleatum* and Gal-GalNAc overexpressed on breast cancer cells. *In vivo* animal results strongly support that *F. nucleatum* colonization in tumors would significantly promote the development of tumor chemoresistance to different chemotherapeutic drugs, possibly due to the activated autophagy pathway of breast cancer cells to reduce their responses to chemotherapeutics. With a deep understanding of the relationship between *F. nucleatum* and breast cancer, eliminating tumor-colonizing *F. nucleatum* may be a strategy to improve current chemotherapy for *F. nucleatum*-colonized breast cancer.

Although antibiotics continue to be the foremost choice for eliminating bacteria, it is worth noting that effectively eliminating tumor-resident bacteria often necessitates the use of high doses and frequent administration. One concern is their negative

effect on the healthy intestinal microbiota and their ability to contribute to the emergence of multidrug-resistant strains. One would ideally want to develop a targeted delivery system to selectively eradicate bacteria within tumors. Inspired by the accumulation of *F. nucleatum* in breast cancer mediated by the interactions between the membrane protein Fap-2 in *F. nucleatum* and Gal-GalNAc overexpressed in breast cancer cells, we developed *F. nucleatum*-mimetic nanovehicles by fusing FM with liposomes for targeted delivery of antibiotics to *F. nucleatum*-infected tumors. Interestingly, the obtained LipoFM encapsulated with the antibiotic colistin could successfully eliminate intratumoral *F. nucleatum* and restore the therapeutic efficacy of chemotherapy in an *F. nucleatum*-infected mouse breast tumor model due to its superior tumor-specific targeting and retention ability.

Metastasis is the major cause of death in patients with breast cancer. It has been reported that some tumor-colonizing bacteria, such as *Streptococcus* and *Staphylococcus*, could accelerate cancer metastasis.[24] We further loaded LipoFM with Doxy, a broad-spectrum antibiotic, and demonstrated that i.v. injection of Doxy-LipoFM could effectively kill intratumoral microflora and inhibit the lung metastasis of breast cancer tumors containing different types of bacteria. As the result, Doxy-LipoFM could remarkably improve the therapeutic efficacy of the standard CMF chemotherapy for breast cancer, achieving outstanding therapeutic effects in the breast tumor model infected with a mixture of different types of bacteria.

Our study provided critical insights of the relationship between tumor-colonizing bacteria, tumor progression, and its resistance to chemotherapeutics. In particular, the design of *F. nucleatum*-mimicking nanovehicles utilizing bacterial membrane to target its binding site on tumor cells opens new horizons for specific targeting of bacteria-colonized tumors and selective eliminating of intratumoral microbiota. By doing so, the chemoresistance of bacteria-colonizing breast tumors could be largely relieved, resulting in remarkably enhanced therapeutic efficacies and inhibiting tumor metastasis. Therefore, our work has the potential to revolutionize the current breast cancer treatment. For future clinical applications, it may be essential to analyze the microbes in breast cancer tumors post-surgery and before chemotherapy. For those tumors with overexpression of Gal-GalNAc and high levels of bacterial colonization, they should be treated with antibiotic-loaded *F. nucleatum*-mimetic nanovehicles before chemotherapy is given, so as to achieve the optimal therapeutic outcome. In addition to loading antibiotics, LipoFM also has the potential to be utilized for targeted delivery of chemotherapeutic drugs. Moreover, a deeper comprehension of intratumoral microbes holds the potential to open new avenues for groundbreaking treatment alternatives for individuals battling cancer.

EXPERIMENTAL PROCEDURES

Resource availability

Lead contact

Further information and requests for resources and reagents should be directed to and will be fulfilled by the lead contact, Qian Chen (chenqian@suda.edu.cn).

Materials availability

This study did not generate new unique reagents.

Data and code availability

All data needed to evaluate the conclusion of this work are presented in the paper and the supplemental information. Other data related to this work are available from the lead contact upon reasonable request.

Full experimental procedures are provided in the supplemental information.

SUPPLEMENTAL INFORMATION

Supplemental information can be found online at https://doi.org/10.1016/j.chempr.2024.01.030.

ACKNOWLEDGMENTS

This article was partially supported by the National Research Programs of China (2020YFA0211100 and 2022YFA1206500), the National Natural Science Foundation of China (52032008, 21927803, 52250002, 52325106, and 52273013), the Suzhou Key Laboratory of Nanotechnology and Biomedicine, the Collaborative Innovation Center of Suzhou Nano Science and Technology, and the 111 Program from the Ministry of Education of China.

AUTHOR CONTRIBUTIONS

Conceptualization, L.C., J.S., Q.C., and Z.L.; methodology, L.C., Z.K., Z.Z., L.Z., Z.X., and Q.Z.; investigation, L.C., Z.Z., H.F., J.Z., Y.W., Y.Y., and Q.C.; writing – original draft, L.C., J.S., Z.Z., and Q.Z.; writing – review & editing, L.C., Q.C., and Z.L.; supervision, Q.C., Z.L., and Y.Y.; funding acquisition, Q.C. and Y.Y.

DECLARATION OF INTERESTS

The authors declare no competing interests.

Received: September 11, 2023
Revised: December 18, 2023
Accepted: January 31, 2024
Published: February 23, 2024

REFERENCES

1. Kuerer, H.M., Smith, B.D., Krishnamurthy, S., Yang, W.T., Valero, V., Shen, Y., Lin, H., Lucci, A., Boughey, J.C., White, R.L., et al. (2022). Eliminating breast surgery for invasive breast cancer in exceptional responders to neoadjuvant systemic therapy: a multicentre, single-arm, phase 2 trial. Lancet Oncol. *23*, 1517–1524.

2. Tolaney, S.M., Tarantino, P., Graham, N., Tayob, N., Parè, L., Villacampa, G., Dang, C.T., Yardley, D.A., Moy, B., Marcom, P.K., et al. (2023). Adjuvant paclitaxel and trastuzumab for node-negative, HER2-positive breast cancer: final 10-year analysis of the open-label, single-arm, phase 2 APT trial. Lancet Oncol. *24*, 273–285.

3. Britt, K.L., Cuzick, J., and Phillips, K.A. (2020). Key steps for effective breast cancer prevention. Nat. Rev. Cancer *20*, 417–436.

4. Giaquinto, A.N., Sung, H., Miller, K.D., Kramer, J.L., Newman, L.A., Minihan, A., Jemal, A., and Siegel, R.L. (2022). Breast cancer statistics, 2022. CA Cancer J. Clin. *72*, 524–541.

5. Autier, P., Boniol, M., Gavin, A., and Vatten, L.J. (2011). Breast cancer mortality in neighbouring European countries with different levels of screening but similar access to treatment: trend analysis of WHO mortality database. BMJ *343*, d4411.

6. Joko-Fru, W.Y., Miranda-Filho, A., Soerjomataram, I., Egue, M., Akele-Akpo, M.T., N'da, G., Assefa, M., Buziba, N., Korir, A., Kamate, B., et al. (2020). Breast cancer survival in sub-Saharan Africa by age, stage at diagnosis and human development index: A population-based registry study. Int. J. Cancer *146*, 1208–1218.

7. Weigelt, B., Peterse, J.L., and van 't Veer, L.J. (2005). Breast cancer metastasis: markers and models. Nat. Rev. Cancer *5*, 591–602.

8. Liang, Y., Zhang, H., Song, X., and Yang, Q. (2020). Metastatic heterogeneity of breast cancer: molecular mechanism and potential therapeutic targets. Semin. Cancer Biol. *60*, 14–27.

9. Hassan, M.S.U., Ansari, J., Spooner, D., and Hussain, S.A. (2010). Chemotherapy for breast cancer (Review). Oncol. Rep. *24*, 1121–1131.

10. Anampa, J., Makower, D., and Sparano, J.A. (2015). Progress in adjuvant chemotherapy for breast cancer: an overview. BMC Med. *13*, 195.

11. Nardin, S., Mora, E., Varughese, F.M., D'Avanzo, F., Vachanaram, A.R., Rossi, V., Saggia, C., Rubinelli, S., and Gennari, A. (2020). Breast cancer survivorship, quality of life, and late toxicities. Front. Oncol. *10*, 864.

12. Ji, X., Lu, Y., Tian, H., Meng, X., Wei, M., and Cho, W.C. (2019). Chemoresistance mechanisms of breast cancer and their countermeasures. Biomed. Pharmacother. *114*, 108800.

13. Chuthapisith, S., Eremin, J., El-Sheemey, M., and Eremin, O. (2010). Breast cancer chemoresistance: emerging importance of cancer stem cells. Surg. Oncol. *19*, 27–32.

14. O'Reilly, E.A., Gubbins, L., Sharma, S., Tully, R., Guang, M.H.Z., Weiner-Gorzel, K., McCaffrey, J., Harrison, M., Furlong, F., Kell, M., et al. (2015). The fate of chemoresistance in triple negative breast cancer (TNBC). BBA Clin. *3*, 257–275.

15. Nejman, D., Livyatan, I., Fuks, G., Gavert, N., Zwang, Y., Geller, L.T., Rotter-Maskowitz, A., Weiser, R., Mallel, G., Gigi, E., et al. (2020). The human tumor microbiome is composed of tumor type–specific intracellular bacteria. Science *368*, 973–980.

16. Matson, V., Fessler, J., Bao, R., Chongsuwat, T., Zha, Y., Alegre, M.L., Luke, J.J., and Gajewski, T.F. (2018). The commensal microbiome is associated with anti–PD-1 efficacy in metastatic melanoma patients. Science *359*, 104–108.

17. Gopalakrishnan, V., Spencer, C.N., Nezi, L., Reuben, A., Andrews, M.C., Karpinets, T.V., Prieto, P.A., Vicente, D., Hoffman, K., Wei, S.C., et al. (2018). Gut microbiome modulates

response to anti–PD-1 immunotherapy in melanoma patients. Science *359*, 97–103.

18. Riquelme, E., Zhang, Y., Zhang, L., Montiel, M., Zoltan, M., Dong, W., Quesada, P., Sahin, I., Chandra, V., San Lucas, A., et al. (2019). Tumor microbiome diversity and composition influence pancreatic cancer outcomes. Cell *178*, 795–806.e12.

19. Yu, T., Guo, F., Yu, Y., Sun, T., Ma, D., Han, J., Qian, Y., Kryczek, I., Sun, D., Nagarsheth, N., et al. (2017). Fusobacterium nucleatum promotes chemoresistance to colorectal cancer by modulating autophagy. Cell *170*, 548–563.e16.

20. Kostic, A.D., Chun, E., Robertson, L., Glickman, J.N., Gallini, C.A., Michaud, M., Clancy, T.E., Chung, D.C., Lochhead, P., Hold, G.L., et al. (2013). Fusobacterium nucleatum potentiates intestinal tumorigenesis and modulates the tumor-immune microenvironment. Cell Host Microbe *14*, 207–215.

21. Casasanta, M.A., Yoo, C.C., Udayasuryan, B., Sanders, B.E., Umaña, A., Zhang, Y., Peng, H., Duncan, A.J., Wang, Y., Li, L., et al. (2020). Fusobacterium nucleatum host-cell binding and invasion induces IL-8 and CXCL1 secretion that drives colorectal cancer cell migration. Sci. Signal. *13*, eaba9157.

22. Parhi, L., Alon-Maimon, T., Sol, A., Nejman, D., Shhadeh, A., Fainsod-Levi, T., Yajuk, O., Isaacson, B., Abed, J., Maalouf, N., et al. (2020). Breast cancer colonization by Fusobacterium nucleatum accelerates tumor growth and metastatic progression. Nat. Commun. *11*, 3259.

23. Bullman, S., Pedamallu, C.S., Sicinska, E., Clancy, T.E., Zhang, X., Cai, D., Neuberg, D., Huang, K., Guevara, F., Nelson, T., et al. (2017). Analysis of Fusobacterium persistence and antibiotic response in colorectal cancer. Science *358*, 1443–1448.

24. Fu, A., Yao, B., Dong, T., Chen, Y., Yao, J., Liu, Y., Li, H., Bai, H., Liu, X., Zhang, Y., et al. (2022). Tumor-resident intracellular microbiota promotes metastatic colonization in breast cancer. Cell *185*, 1356–1372.e26.

25. Cameron, D., Morden, J.P., Canney, P., Velikova, G., Coleman, R., Bartlett, J., Agrawal, R., Banerji, J., Bertelli, G., Bloomfield, D., et al. (2017). Accelerated versus standard epirubicin followed by cyclophosphamide, methotrexate, and fluorouracil or capecitabine as adjuvant therapy for breast cancer in the randomised UK TACT2 trial (CRUK/05/19): a multicentre, phase 3, open-label, randomised, controlled trial. Lancet Oncol. *18*, 929–945.

26. Ternes, D., Tsenkova, M., Pozdeev, V.I., Meyers, M., Koncina, E., Atatri, S., Schmitz, M., Karta, J., Schmoetten, M., Heinken, A., et al. (2022). The gut microbial metabolite formate exacerbates colorectal cancer progression. Nat. Metab. *4*, 458–475.

27. Chen, S., Zhang, L., Li, M., Zhang, Y., Sun, M., Wang, L., Lin, J., Cui, Y., Chen, Q., Jin, C., et al. (2022). Fusobacterium nucleatum reduces METTL3-mediated m6A modification and contributes to colorectal cancer metastasis. Nat. Commun. *13*, 1248.

28. Galeano Niño, J.L., Wu, H., LaCourse, K.D., Kempchinsky, A.G., Baryiames, A., Barber, B., Futran, N., Houlton, J., Sather, C., Sicinska, E., et al. (2022). Effect of the intratumoral microbiota on spatial and cellular heterogeneity in cancer. Nature *611*, 810–817.

29. Brentnall, M., Rodriguez-Menocal, L., De Guevara, R.L., Cepero, E., and Boise, L.H. (2013). Caspase-9, caspase-3 and caspase-7 have distinct roles during intrinsic apoptosis. BMC Cell Biol. *14*, 32.

30. Tanida, I., Ueno, T., and Kominami, E. (2008). LC3 and autophagy. Methods Mol. Biol. *445*, 77–88.

31. Du, B., and Shim, J.S. (2016). Targeting epithelial–mesenchymal transition (EMT) to overcome drug resistance in cancer. Molecules *21*, 965.

32. Gelfo, V., Romaniello, D., Mazzeschi, M., Sgarzi, M., Grilli, G., Morselli, A., Manzan, B., Rihawi, K., and Lauriola, M. (2020). Roles of IL-1 in cancer: from tumor progression to resistance to targeted therapies. Int. J. Mol. Sci. *21*.

33. Hutchings, M.I., Truman, A.W., and Wilkinson, B. (2019). Antibiotics: past, present and future. Curr. Opin. Microbiol. *51*, 72–80.

34. Zhang, G., Wang, Q., Tao, W., Jiang, W., Elinav, E., Wang, Y., and Zhu, S. (2022). Glucosylated nanoparticles for the oral delivery of antibiotics to the proximal small intestine protect mice from gut dysbiosis. Nat. Biomed. Eng. *6*, 867–881.

35. Jiang, L., Zhu, Y., Luan, P., Xu, J., Ru, G., Fu, J.G., Sang, N., Xiong, Y., He, Y., Lin, G.Q., et al. (2021). Bacteria-anchoring hybrid liposome capable of absorbing multiple toxins for antivirulence therapy of Escherichia coli infection. ACS Nano *15*, 4173–4185.

36. Liu, Z., Wang, F., Liu, X., Sang, Y., Zhang, L., Ren, J., and Qu, X. (2021). Cell membrane–camouflaged liposomes for tumor cell–selective glycans engineering and imaging in vivo. Proc. Natl. Acad. Sci. USA *118*, e2022769118.

37. Szoka, F., and Papahadjopoulos, D. (1978). Procedure for preparation of liposomes with large internal aqueous space and high capture by reverse-phase evaporation. Proc. Natl. Acad. Sci. USA *75*, 4194–4198.

38. Nation, R.L., and Li, J. (2009). Colistin in the 21st century. Curr. Opin. Infect. Dis. *22*, 535–543.

39. Wang, J., Li, P., Yu, Y., Fu, Y., Jiang, H., Lu, M., Sun, Z., Jiang, S., Lu, L., and Wu, M.X. (2020). Pulmonary surfactant–biomimetic nanoparticles potentiate heterosubtypic influenza immunity. Science *367*, eaau0810.

40. Ringgaard, L., Melander, F., Eliasen, R., Henriksen, J.R., Jølck, R.I., Engel, T.B., Bak, M., Fliedner, F.P., Kristensen, K., Elema, D.R., et al. (2020). Tumor repolarization by an advanced liposomal drug delivery system provides a potent new approach for chemo-immunotherapy. Sci. Adv. *6*, eaba5628.

41. Yu, K.D., Huang, S., Zhang, J.X., Liu, G.Y., and Shao, Z.M. (2013). Association between delayed initiation of adjuvant CMF or anthracycline-based chemotherapy and survival in breast cancer: a systematic review and meta-analysis. BMC Cancer *13*, 240.

42. Ponomarenko, D.M., Gabai, V.L., Sufianov, A.A., Kolesnikov, S.I., and Shneider, A.M. (2020). Response of a chemo-resistant triple-negative breast cancer patient to a combination of p62-encoding plasmid, Elenagen, and CMF chemotherapy. Oncotarget *11*, 294–299.

Chem, Volume *10*

Supplemental information

Fusobacterium nucleatum-mimicking nanovehicles to overcome chemoresistance for breast cancer treatment by eliminating tumor-colonizing bacteria

Linfu Chen, Jingjing Shen, Zheyu Kang, Zemin Zhang, Zixuan Zheng, Lin Zhang, Zhisheng Xiao, Qiang Zhang, Huapan Fang, Jun Zhou, Yudong Wang, Yang Yang, Zhuang Liu, and Qian Chen

Supplemental Figures

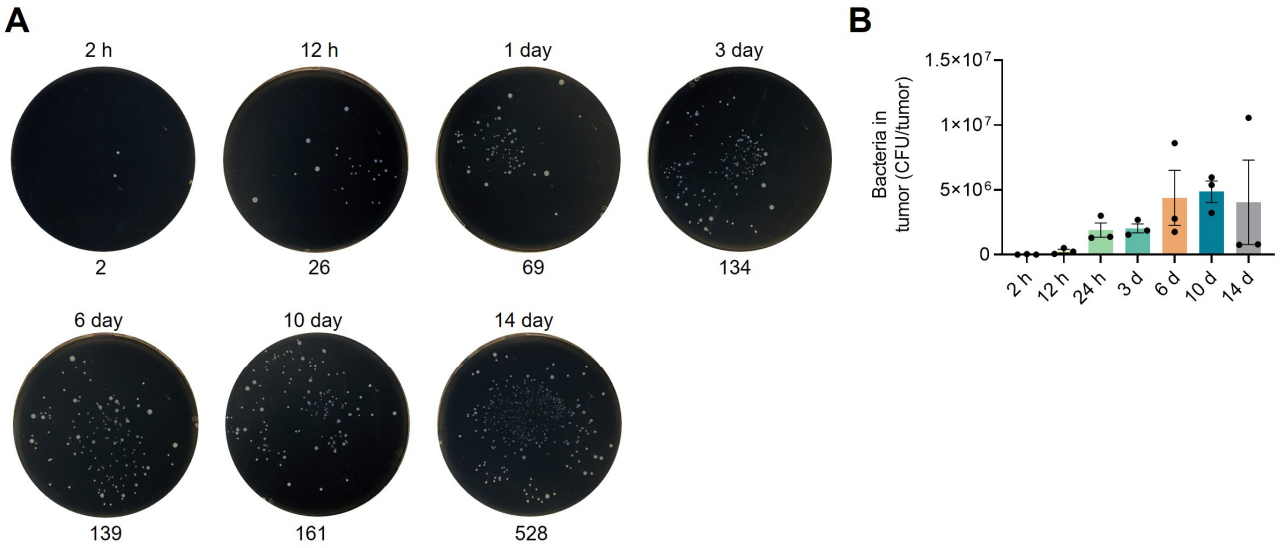

Figure S1. The abundance of *F. nucleatum* in 4T1 tumors. A) Colony plate images and B) the statistical analysis of CFU showing the intratumoral *F. nucleatum* of mice with different treatments as indicated. The black number in each picture indicates the number of CFU in each plate. The dilution of homogenized tumor solution was 20,000. Data are presented as the mean ± s.e.m. (n = 3).

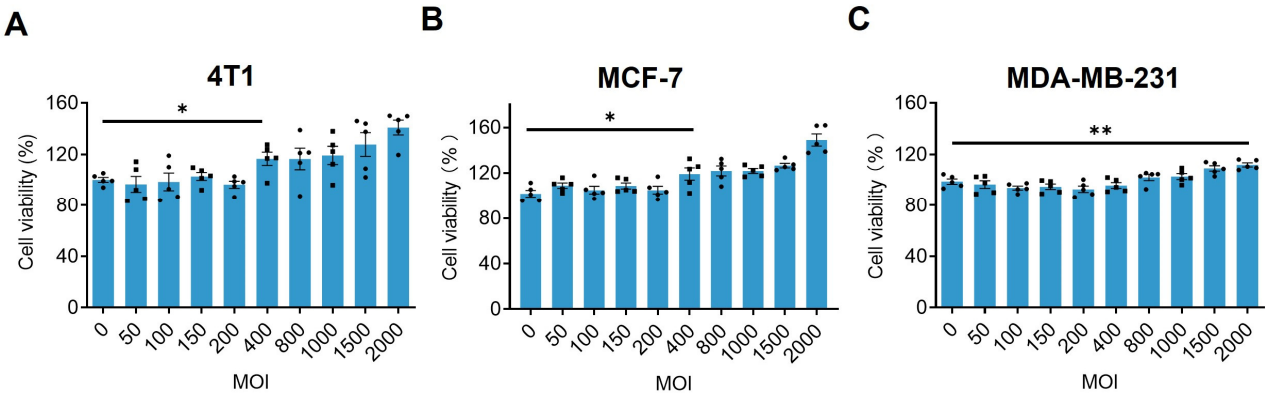

Figure S2. The relative viabilities of cells after incubated with different concentration of *F. nucleatum* for 24 hours. A) Relative viabilities of 4T1 cells, B) MCF-7 cells and (C) MDA-MB-231 cells. Data are presented as mean ± s.e.m. (n = 5).

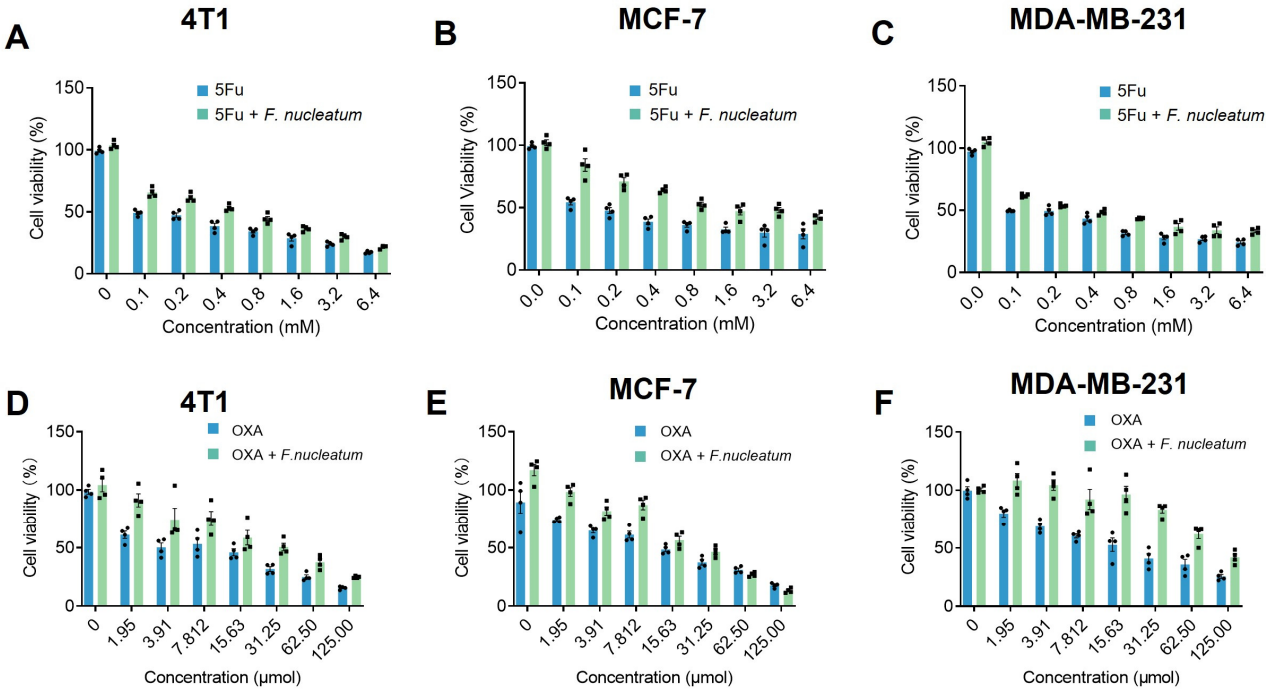

Figure S3. The relative viabilities of cells with different treatments. A-F) Relative viabilities of 4T1 cells (A, D), MCF-7 cells (B, E) and MDA-MB-231 cells (C, F) with or without *F. nucleatum* infection after incubated with different concentrations of 5Fu (A-C) or OXA (D-F) for 24 h.

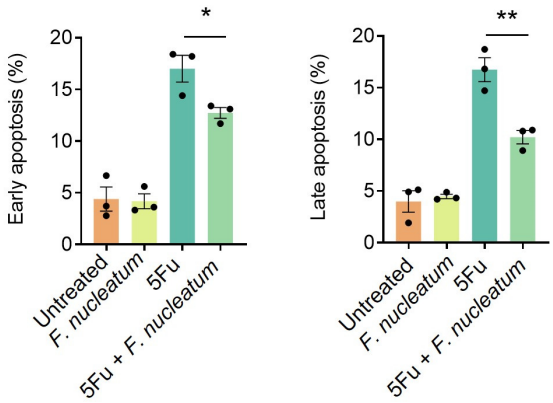

Figure S4. Percentages of cell apoptosis after different treatments as indicated. Data are presented as the mean ± s.e.m. (n = 3). Statistical significance was calculated via two-tailed Student's t test in GraphPad Prism. *p < 0.05; **p < 0.01; ***p < 0.001; ****p < 0.0001.

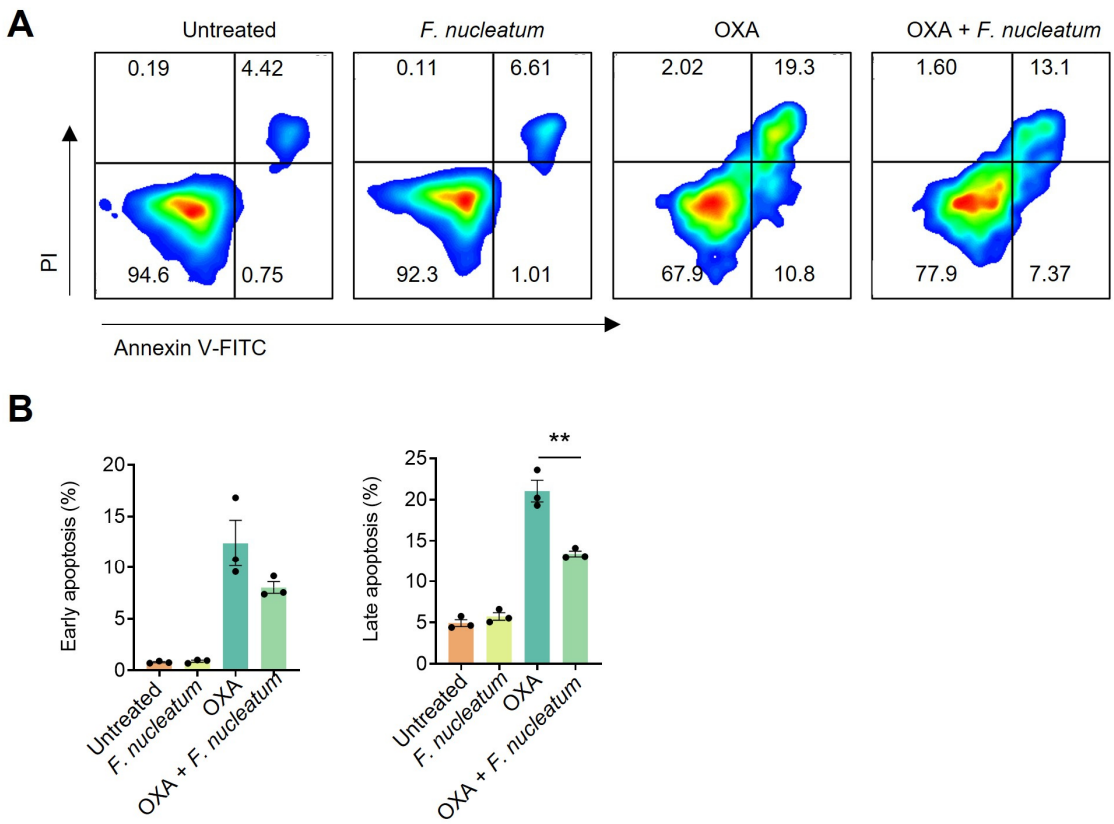

Figure S5. Cell apoptosis after treated with OXA and *F. nucleatum*. A) Representative flow cytometric analysis images and (B) percentages of cell apoptosis after different treatments as indicated. Data are presented as the mean ± s.e.m. (n = 3). Statistical significance was calculated via two-tailed Student's t test (B) in GraphPad Prism. *p < 0.05; **p < 0.01; ***p < 0.001; ****p < 0.0001.

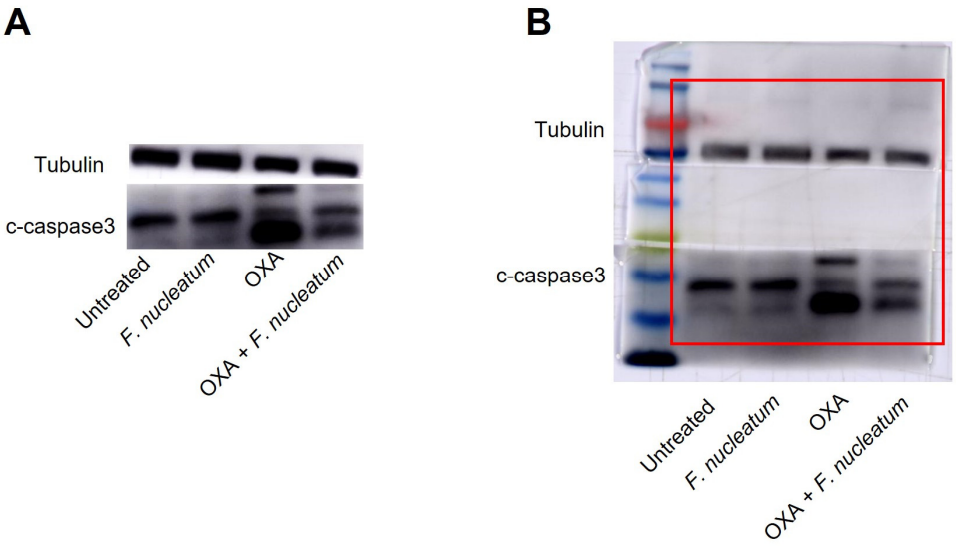

Figure S6. The expression of c-caspase 3 after different treatments. A) Western blotting images showing the expression of c-caspase3 in 4T1 cells after different treatments as indicated. B) The raw data of Western blotting gel in (A).

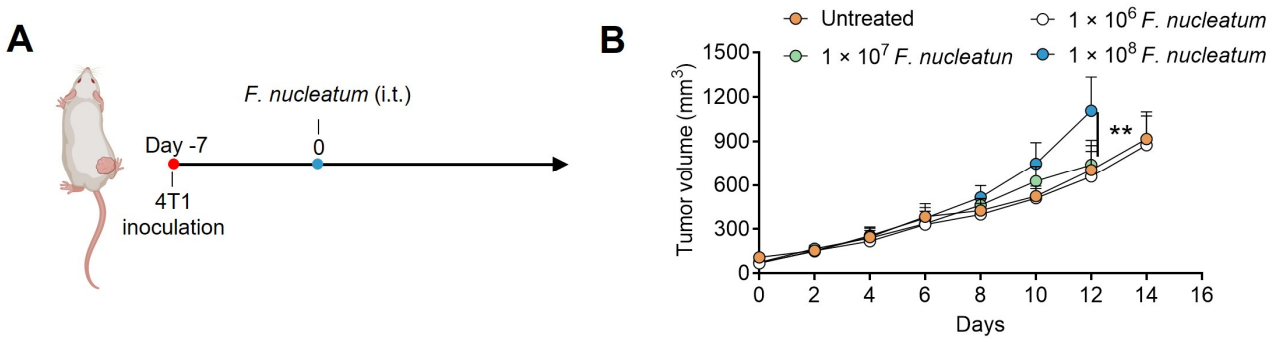

Figure S7. The effect of *F. nucleatum* on tumor growth. A) Timeline of treatments of mice bearing subcutaneous 4T1 tumors. B) Average tumor growth curves of 4T1 tumors in mice with various treatments as indicated. Growth curves were stopped when the tumor volumes were larger than 1000 mm^3 in the corresponding group. Data are presented as the mean ± s.e.m. (n = 6). Statistical significance was calculated via two-tailed Student's t test (B) in GraphPad Prism. *p < 0.05; **p < 0.01; ***p < 0.001; ****p < 0.0001.

Figure S8. Digital photograph of mouse treated with 1 × 10^9 CFU *F. nucleatum*.

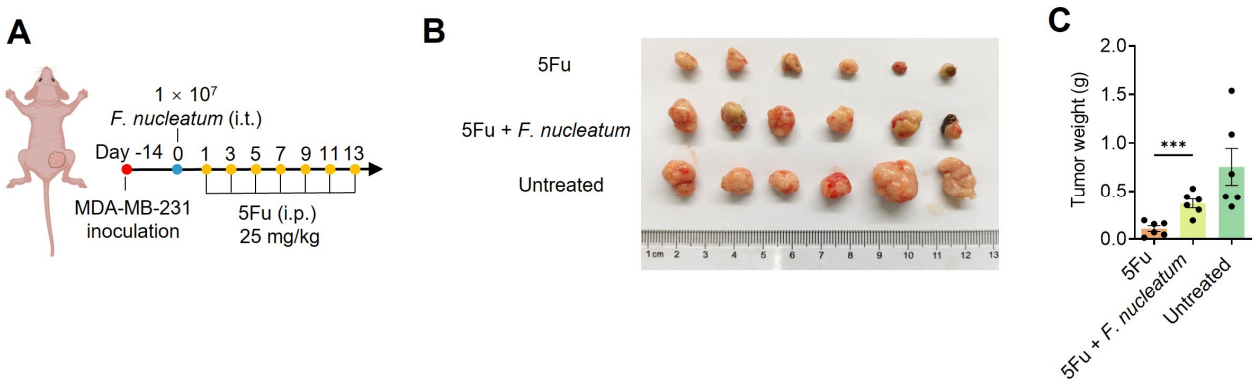

Figure S9. *F. nucleatum* promotes chemoresistance in MDA-MB-231 tumors. A) Schematic illustrating the design of animal experiments in MDA-MB-231 tumor-bearing mice. B, C) Images (B) and weights (C) of MDA-MB-231 tumors harvested from mice after different treatments as indicated. Data are presented as the mean ± s.e.m. (n = 6). Statistical significance was calculated via two-tailed Student's-t test (C) in GraphPad Prism. *p < 0.05; **p < 0.01; ***p < 0.001; ****p < 0.0001.

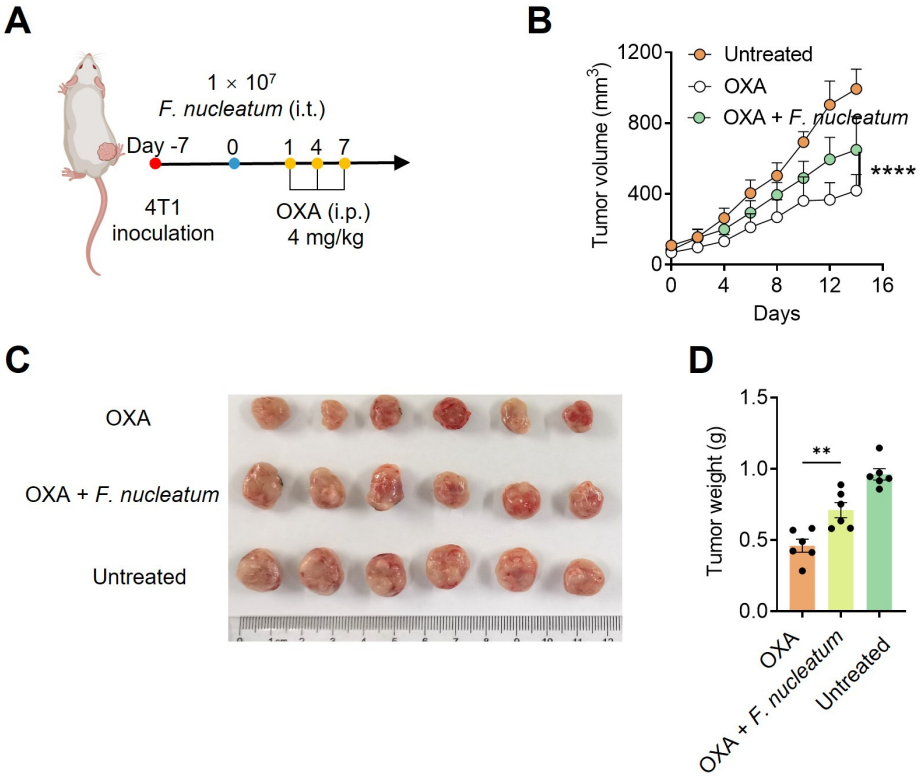

Figure S10. *F. nucleatum* promotes chemoresistance in 4T1 tumors. A) Schematic illustrating the design of animal experiments in 4T1 tumor-bearing mice, B-D) average tumor growth curves (B), images (C) and weights (D) of 4T1 tumors harvested from mice after different treatments as indicated. Data are presented as the mean ± s.e.m. (n = 6). Statistical significance was calculated via two-tailed Student's-t test (D) and two-way ANOVA (B) in GraphPad Prism. *p < 0.05; **p < 0.01; ***p < 0.001; ****p < 0.0001.

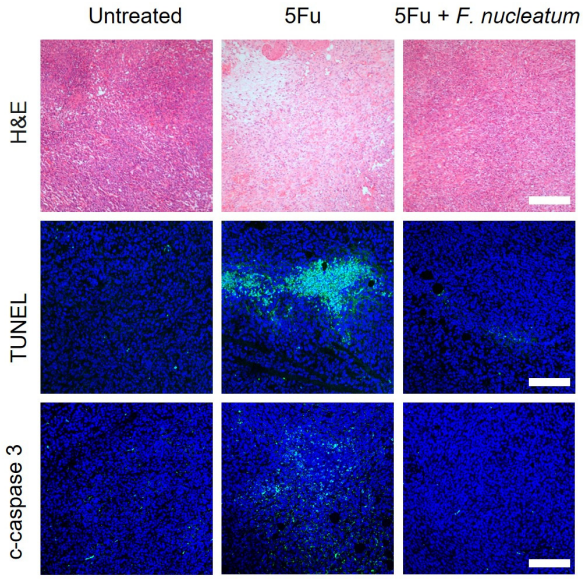

Figure S11. H&E, TUNEL and c-caspase 3 staining images of tumors collected from mice with different treatments on day 14. Scale bar, 200 μm for H&E staining images and 100 μm for TUNEL and c-caspase 3 staining images.

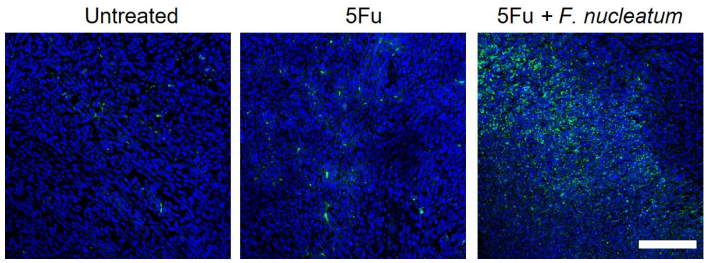

Figure S12. The immunofluorescence staining images of LC 3 in tumors collected on day 14 after different treatment as indicated. Scale bar, 100 μm.

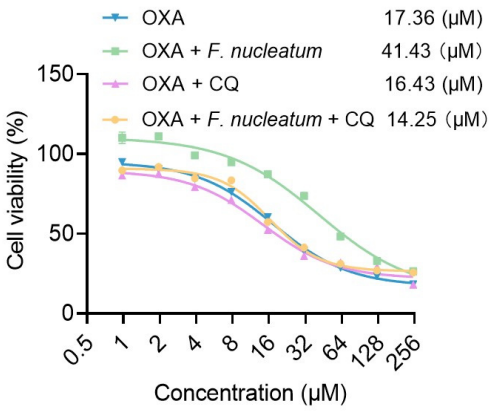

Figure S13. Relative viabilities of 4T1 cells infected with *F. nucleatum* with different treatments as indicated.

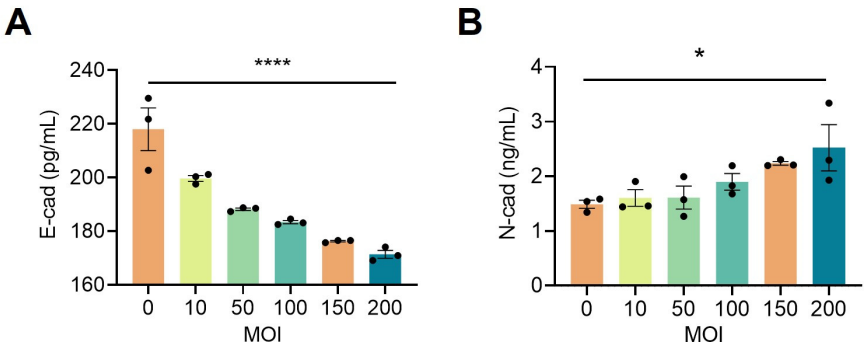

Figure S14. The effect of *F. nucleatum* on tumor epithelial-mesenchymal transition. The contents of E-cadherin (A) and N-cadherin (B) in 4T1 cells after cultured with different concentrations of *F. nucleatum* for 24 hours. Data are presented as the mean ± s.e.m. (n = 3). Statistical significance was calculated via calculated via one-way ANOVA in GraphPad Prism. *p < 0.05; **p < 0.01; ***p < 0.001; ****p < 0.0001.

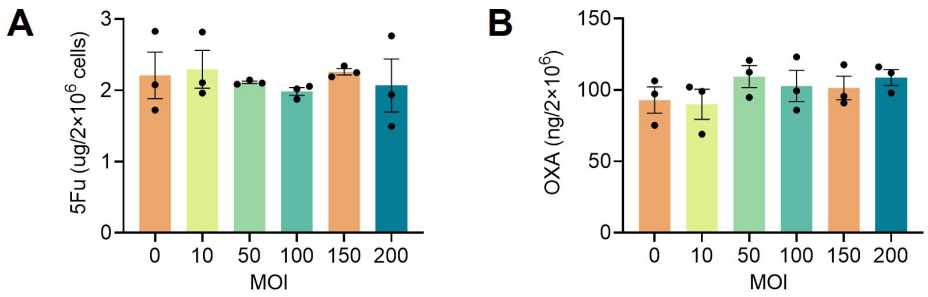

Figure S15. The effect of *F. nucleatum* on uptake of 5Fu and OXA by cancer cells. The intracellular contents of 5Fu (A) and OXA (B) in 4T1 cells 24 hours after infected with different concentrations of *F. nucleatum*. Data are presented as the mean ± s.e.m. (n = 3).

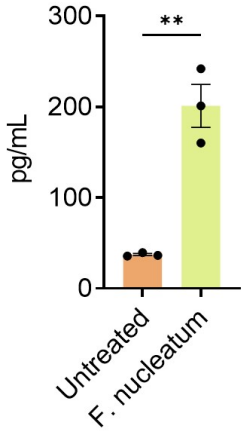

Figure S16. The levels of IL-1β secreted from 4T1 cells with *F. nucleaum* infection. Data are presented as the mean ± s.e.m. (n = 3). Statistical significance was calculated via two-tailed Student's t test in GraphPad Prism. *p < 0.05; **p < 0.01; ***p < 0.001; ****p< 0.0001.

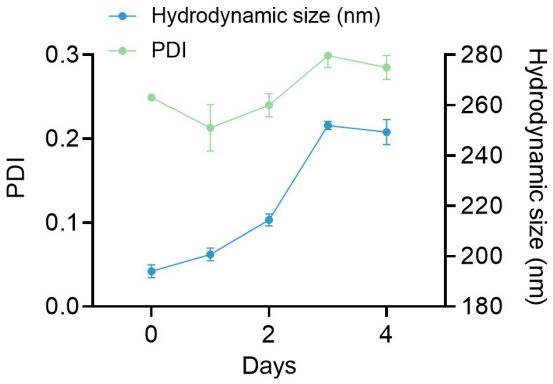

Figure S17. Time lapsed hydrodynamic size and PDI of FM. Data are presented as mean ± s.e.m. (n = 3).

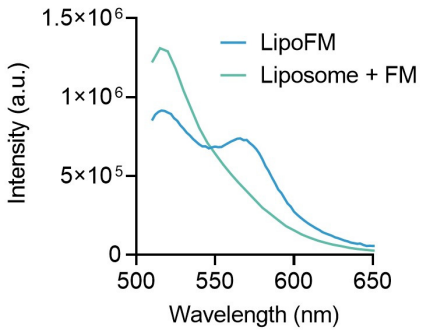

Figure S18. Fluorescence spectra of fused liposomes labeled with FITC and FM labeled with TRITC.

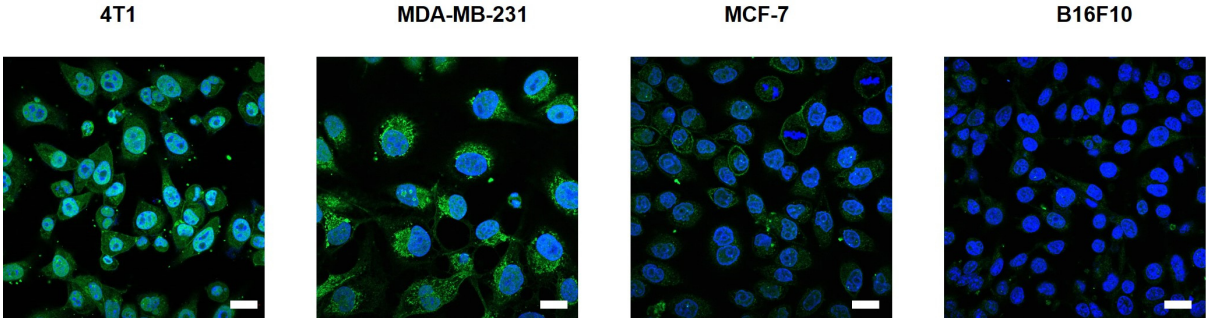

Figure S19. Representative immunofluorescent staining images showing the levels of Gal-GalNAc (Green) in 4T1, MDA-MB-231, MCF-7 and B16F10 cells. Scare bar, 20 μm.

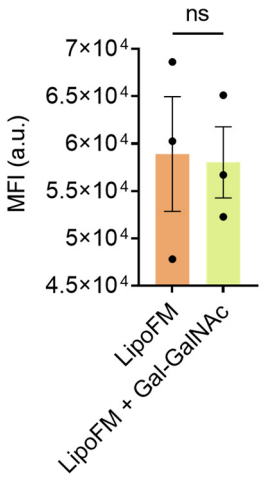

Figure S20. Flow cytometry analysis of B16F10 cells incubated with DiD-LipoFM or DiD-LipoFM + Gal-GalNAc for 24 hours. Statistical analysis of DiD intensity in B16F10 cells. Data are presented as mean ± s.e.m. (n = 3).

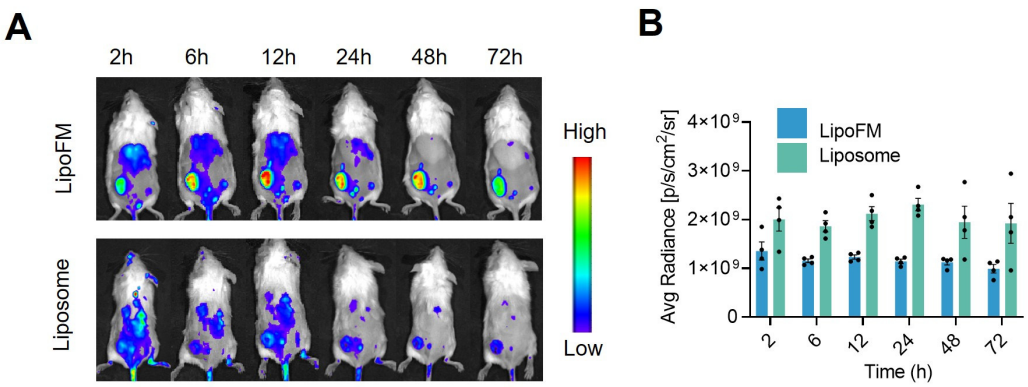

Figure S21. The tumor targeting ability of LipoFM. A) In vivo fluorescence imaging of mice bearing 4T1 tumors after intravenous injection with DiR-labeled Liposome or DiR-labeled LipoFM. B) Statistical analysis of the average DiR fluorescence signals in 4T1 tumors based on the images in (A). Data are presented as mean ± s.e.m. (n = 4).

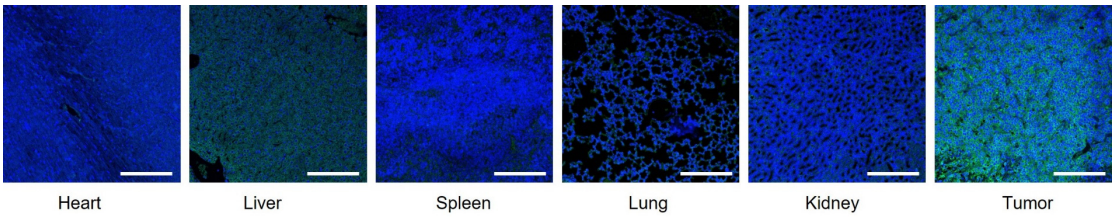

Figure S22. Representative immunofluorescence staining images of the level of Gal-GalNAc (Green) in heart, liver, spleen, lung, kidney and 4T1 tumor. Scale bar, 200 μm.

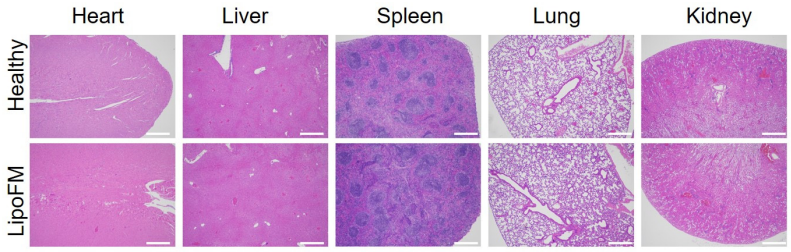

Figure S23. The H&E staining images of hearts, livers, spleens, lungs, and kidneys of the mice treated with LipoFM. Scale bar, 500 μm.

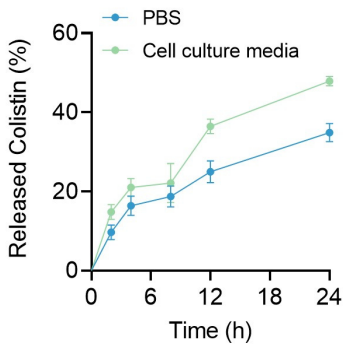

Figure S24. The release profiles of colistin from the Colistin-LipoFM incubated in PBS or cell culture media. Data are presented as mean ± s.e.m. (n = 3).

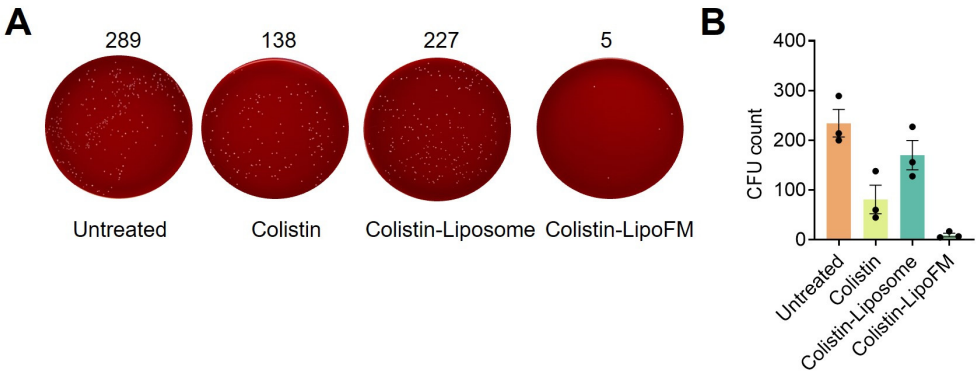

Figure S25. The abundance of intracellular *F. nulceatum* after different treatments. A) Colony plate images and (B) statistical analysis of the colony-forming units showing the abundance of *F. nucleatum* in 4T1 cells after different treatments for 24 hours. Data are presented as mean ± s.e.m. (n = 3).

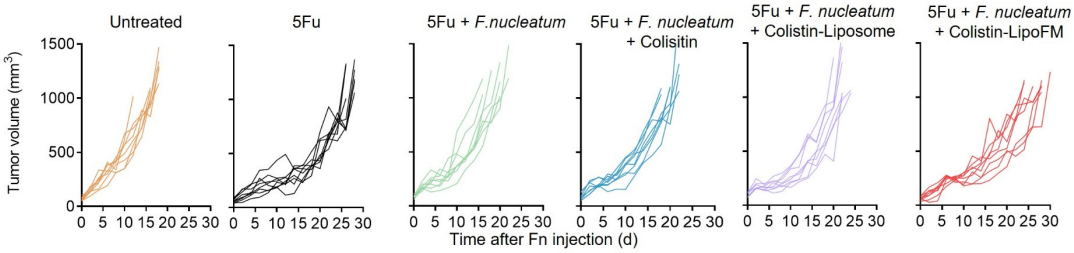

Figure S26. The individual tumor growth curves of 4T1 tumors in mice with various treatments as indicated in Figure 5H (n = 8).

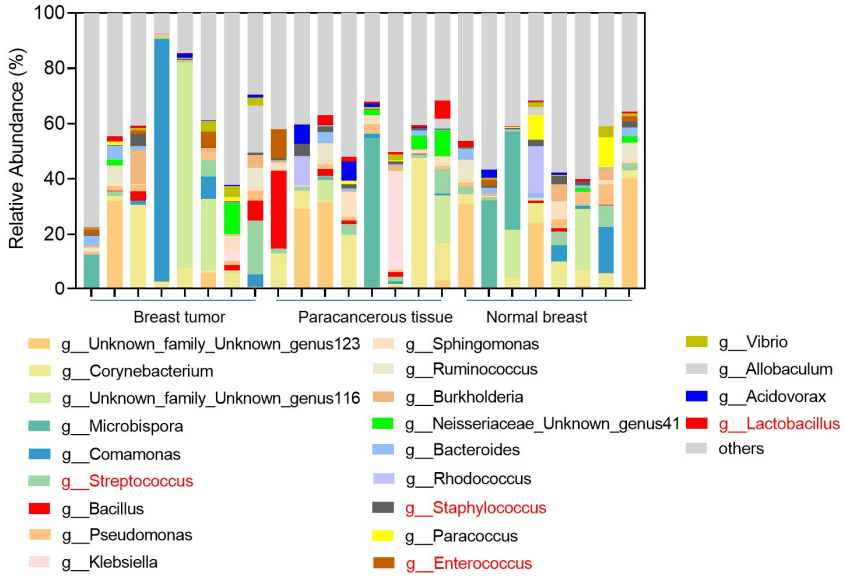

Figure S27. Genus-level microbial composition of paired breast primary tumors, paracancerous tissues and normal breast tissues.

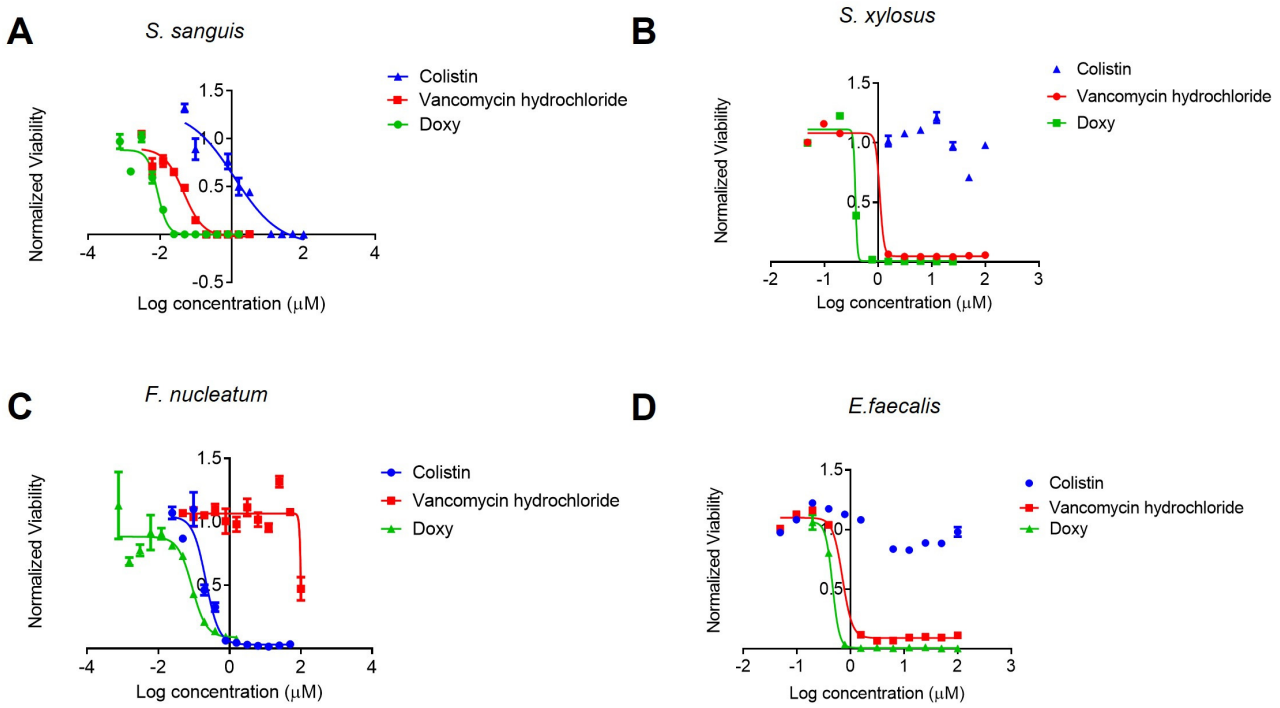

Figure S28. The anti-bacteria ability of antibiotics. The relative viabilities of *S.sanguis* (A), *S.xylosus* (B), *F. nucleatum* (C) and *E. faecalis* (D) treated with different concentrations of colistin, vancomycin hydrochloride, doxy for 24 h. Data are presented as mean ± s.e.m. (n = 3).

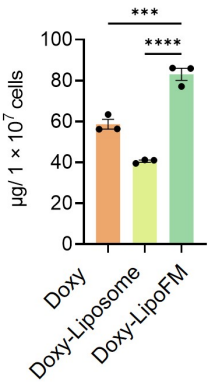

Figure S29. The concentration of Doxy in 4T1 cells after co-cultured with different formations. Data are presented as mean ± s.e.m. (n = 3).

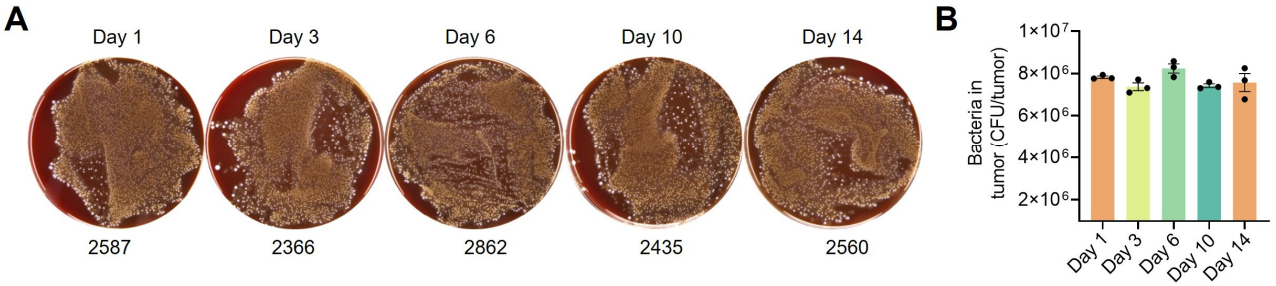

Figure S30. Bacterial colonization in tumors. A, B) Colony plate images (A) and the statistical analysis of CFU (B) showing the abundance of bacteria in tumors harvested on days 1, 3, 6, 10 and 14 post i.t. injection of bacteria. The dilution of homogenized solution was 3000. Data are presented as mean ± s.e.m. (n = 3).

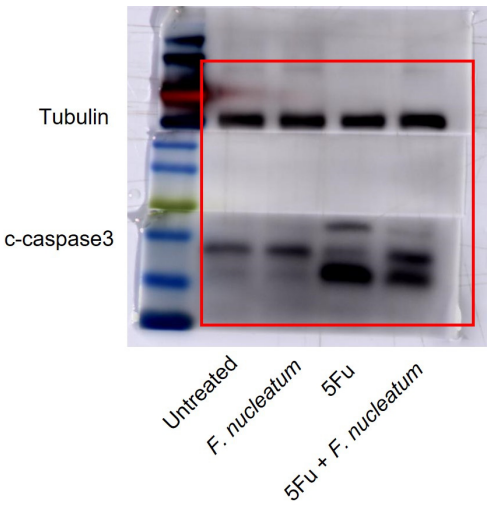

Figure S31. The raw data of the western blotting of Tubulin and c-caspase 3 in Figure 3b.

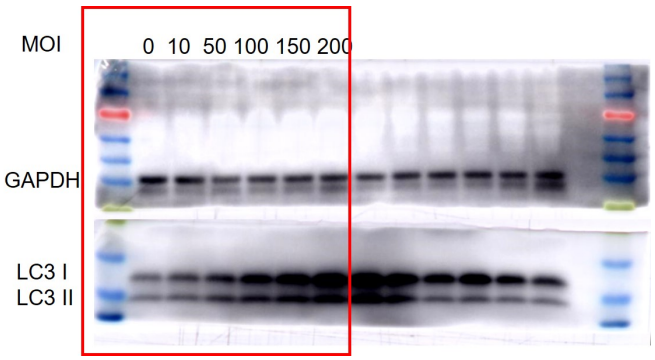

Figure S32. The raw data of the western blotting of LC 3 in Figure 3F.

Table S1: Information of human breast tumor samples.

	Cancer type	Sample type
Sample 1	Invasive carcinoma of right breast	Cancer Paracancer Norm Tissue
Sample 2	Invasive carcinoma of left breast	Cancer Paracancer Norm Tissue
Sample 3	Invasive carcinoma of right breast	Cancer Paracancer Norm Tissue
Sample 4	Intraductal carcinoma of right breast	Cancer Paracancer Norm Tissue
Sample 5	Intraductal carcinoma of right breast	Cancer Paracancer Norm Tissue
Sample 6	Invasive carcinoma of left breast	Cancer Paracancer Norm Tissue
Sample 7	Invasive carcinoma of left breast	Cancer Paracancer Norm Tissue
Sample 8	Invasive carcinoma of right breast	Cancer Paracancer Norm Tissue

Supplemental experimental procedures

Materials, cell lines, bacterial strains, and animals

Lipids including 1,2-dipalmitoyl-sn-glycero-3-phosphocholine (DPPC) and polyethylene glycol-2000 conjugated 1,2-distearoyl-sn-glycero-3-phosphoethanolamine (DSPE-PEG2000) were purchased from Avanti Polar Lipids. Cholesterol and Fluorescein Isothiocyanate (FITC)-conjugated peanut agglutinin (PNA) were purchased from Sigma Aldrich. 5-Fluorouracil (5Fu), Oxaliplatin (OXA), Cyclophosphamide (CTX), and Methotrexate (MTX) were purchased from TargetMol, USA. 1,1'-Dioctadecyl-3,3,3',3'-Tetramethylindodicarbocyanine,4-Chlorobenzenesulfonate Salt (DiD), 1,1′-dioctadecyl-3,3,3′,3′-tetramethylindotricarbocyanine iodide (DiR), FITC, Colistin, Vancomycin hydrochloride, Doxy, Erythrocin, Crystal violet and Tetramethylrhodamine (TRITC) were purchased from Sangon Biotech Co., Ltd. DSPE-PEG2000-Cy5.5 was purchased from Ponsure. Brain heart infusion (BHI) broth, thiolglycollate medium, Luria–Bertani (LB) medium, and Columbia blood agar base were purchased from Qingdao Hope Biotechnology. Mouse IL-1β ELISA kit (SEKM-0002), mouse E-cadherin ELISA kit (SEKM-0068) and mouse N-cadherin ELISA kit (SEKM-0283) was purchased from Beijing Solarbio Science & Technology Co., Ltd. Tissue microarrays were constructed by Shanghai Zhuoli Biotechnology Co., Ltd (Zhuoli Biotechnology Co,Shanghai, China).

Fusobacterium nucleatum (*F. nucleatum*) (ATCC 25586) was purchased from the China General Microbiological Culture Collection Center, *Enterococcus faecalis* (*E. faecalis*) (ATCC 29212), *Streptococcus sanguis* (*S. sanguis*) (ATCC 10556) and *Staphylococcus xylosus* (*S. xylosus*) (ATCC 29971) were obtained from the Guangdong Microbial Culture Collection Center (GDMCC). *F. nucleatum* and *S. sanguis* were cultured in Thiolglycollate medium at 37 ℃ under anaerobic conditions, *E. faecalis* was cultured in BHI medium at 37 ℃, and *S. xylosus* was cultured in LB medium.

4T1, MCF-7, and MDA-MB-231 cells were purchased from Pricella. Luciferase-transfected 4T1 cells (4T1-luc) were a gift from L. Zhang at Shanghai Jiao Tong University. MCF-7 cells and MDA-MB-231 cells were cultured in DMEM containing 10% FBS and 1% penicillin/streptomycin at 37 ℃ in 5% CO_2. 4T1 cells and 4T1-luc cells were cultured in 1640 medium containing 10% FBS and 1% penicillin/streptomycin at 37 ℃ in 5% CO_2. The culture media were purchased from Procell Life Science&Technology Co., Ltd.

6-8 weeks female BALB/c mice and 6-8 weeks female BALB/c-Nude mice were purchased from Nanjing Pengsheng Biological Technology Co. All animal experiments were performed in compliance with the relevant laws and approved by the Institutional Animal Care and Use Committee of Soochow University (No. ECSU-2019000198).

Preparation of cytoplasmic membranes derived from bacteria

F. nucleatum was cultured in Thiolglycollate Medium at 37 ℃ under anaerobic conditions for 48 hours. Subsequently, the bacteria were harvested by centrifugation at 10,000 × g for 10 minutes at 4 ℃ and washed three times with PBS. The *F. nucleatum* was then resuspended in 10 mL of buffer A containing 1 M sucrose, 0.2 M Tris-HCl, and 2 mg/mL lysozyme, followed by incubation at 37 ℃ with shaking at 120 rpm for 1 hour to obtain spheroplasts. The spheroplasts were recovered by centrifugation at 10,000 × g for 10 minutes and resuspended in 10 mL of Buffer B containing 20 mM Tris-HCl, 50 mM NaCl, 5 mM EDTA, and 20% w/v sucrose. The solution was then sonicated with an ultrasonic power of 300 W 99 times. After sonication, the lysate was subjected to centrifugation at 10,000 × g for 30 minutes, and the supernatant was collected. To isolate specific components, 3 mL of lysate was layered on top of sucrose with a discontinuous gradient (bottom to top: 2.5 mL at 50% w/v, 1.25 mL at 46% w/v, 2.5 mL at 42% w/v, 2.5 mL at 36% w/v, 2.5 mL at 32% w/v, and 2.5 mL at 27% w/v). The gradients were then subjected to centrifugation at 50,000×g for 30 minutes at 4 ℃. Following centrifugation, 1

mL of the cytoplasmic membrane fraction was collected for Sodium dodecyl sulfate-polyacrylamide gel electrophoresis (SDS-PAGE) and silver staining. The same experimental procedure was used to isolate the cytoplasmic membranes of *Escherichia coli*.

Synthesis and characterization of LipoFM

Liposomes were synthesized using the reverse-phase evaporation method according to published literature,[1] and FM-fused liposomes (LipoFM) were obtained from FM and liposomes after co-extrusion through a 200 nm polycarbonate membrane for 30 times with the protein-to-lipid mass ratio of 1:20. The size and zeta potential of LipoFM, FM, and liposomes were measured using a Zetasizer (Malvern). Transmission electron microscopy (TEM) images of LipoFM were obtained with an FEI Tecnai F20 transmission electron microscope operating at an acceleration voltage of 200 kV (FEI company).

Measurements of intracellular delivery and antibacterial ability of LipoFM in tumor cells

To assess the cellular adhesion capability of LipoFM, 1×10^5 4T1 cells were co-cultured with DiD-labeled LipoFM, Colistin-LipoFM + Gal-GalNAc (10 mM Gal-GalNAc), DiD-labeled LipoEM (formed by fusion of liposomes and *Escherichia coli* cytoplasmic membrane), and DiD-labeled liposomes for 24 hours at 37 ℃ with 5% CO_2. After being washed three times with PBS, the cells were suspended in FACS buffer (1% FBS in PBS) for flow cytometry analysis. In a parallel experiment, cells were fixed and stained with DAPI, followed by imaging using a fluorescence microscope.

To investigate the targeted uptake of Colistin-LipoFM in 4T1 cells, the cells were incubated with free colistin, Colistin-Liposome and Colistin-LipoFM with a consistent colistin dosage of 100 μg/mL for 24 hours. Afterward, the cells were lysed for HPLC analysis. The same experimental procedure was employed to assess the uptake of Doxy-LipoFM in 4T1 cells.

To evaluate the anti-*F. nucleatum* ability of Colistin-LipoFM in tumor cells, 4T1 cells infected with *F. nucleatum* were co-cultured with free colistin, Colistin-LipoFM, and Colistin-Liposome with the colistin concentration of 6.76 μg/mL. 24 hours later, the cells were washed and lysed, plated on Columbia blood plates and cultured in an anaerobic environment.

In vivo targeting ability of LipoFM

To assess the tumor targeting capability of LipoFM and liposomes, mice bearing subcutaneous 4T1 tumors were intravenously injected with DiR labeled LipoFM or liposome with the equivalent DiR dose. At 2 h, 6 h, 12 h, 24 h, 48 h, and 72 h, mice were imaged using an in vivo imaging instrument (IVIS). 72 hours later, the mice were sacrificed, and their tumors as well as main organs, including the heart, liver, spleen, lung, and kidney, were harvested for ex vivo fluorescence imaging.

To evaluate the biodistribution of colistin, mice with subcutaneous 4T1 tumors were intravenously administered free colistin, colistin-Liposome, and colistin-LipoFM with the same colistin dose of 15 mg/kg. After 24 hours, the mice were sacrificed, and their tumors and main organs were harvested, weighed, and homogenized in 1 mL solutions composed of water, trichloroacetic acid, Triton X-100, and acetonitrile (in a ratio of 68:4:8:20), and measured by HPLC. Colistin was detected at a wavelength of 205 nm, and the mobile phase consisted of an aqueous Na_2SO_4 solution (30 mM, pH=2.5) and acetonitrile, with a volume ratio of 77:23, and eluted at a flow rate of 1 mL/min. The same experimental procedure was employed to measure the biodistribution of Doxy. The mobile phase consisted of a mixture of water and acetonitrile, with a volume ratio of 60:40, and eluted at a flow rate of 1 mL/min. Doxy was detected at a wavelength of 365 nm.

In vitro antibacterial experiments

F. nucleatum, *S. xylosus*, *S. sanguis*, and *E. faecalis* were added to the liquid culture media at a concentration of 1×10^6 colony-forming units (CFU)/mL. Subsequently, antibiotics including Colistin, Vancomycin hydrochloride, Doxy with various concentration gradients were added and incubated at 37 ℃ for 48 hours, followed by the addition of ten microliters of BacTiter-Glo (G8233) per 30 μL of culture media. The relative viability of bacteria in the presence of different antibiotics was determined in comparison to the control according to the luminescence intensity.

Intratumor CFU counting assay

To assess the antibacterial efficacy of Colistin-LipoFM, the tumors were collected six days after different treatments and homogenized under sterile conditions. The samples were then diluted and plated onto BHI agar plates supplemented with 5 g/L yeast extract, 0.5 g/L L-cysteine hydrochloride, 5 mg/L chlorhematin, 1 μL/L vitamin K1,[2] 4 mg/L vancomycin hydrochloride (Eradication of Gram-positive bacteria), 4 mg/L erythromycin, and 1 mg/L crystal violet (used for the isolation and presumptive identification of *F. nucleatum*).[3,4] The plates were incubated at 37 ℃ in an anaerobic environment for 7 days, and the number of colonies was subsequently recorded using a colony counter. The antibacterial efficacy of Doxy-LipoFM was measured using the similar method, except the bacteria were plated onto Columbia blood agar plates.

DNA extraction, quantification and sequencing of tumor bacteria

DNA was extracted from tissues using the FastPure Blood/Cell/Tissue/Bacteria DNA Isolation Mini Kit (Vazyme) supplemented with 1 mg/mL lysozyme. PBS was used as a surrogate for tissue to undergo the same processing steps as tissue samples, and the final DNA product served as the environmental bacteria control (EBC). The bacterial abundance in tissues was quantified using quantitative polymerase chain reaction (qPCR). Each qPCR reaction included 100 ng of DNA, 0.2 μM primers, and a final concentration of 1× SYBR Green PCR Master Mix. DNA amplification and detection were carried out under the following reaction conditions: initial denaturation at 95 ℃ for 10 min, followed by 40 cycles of denaturation at 95 ℃ for 15 s and annealing/extension at 60 ℃ for 1 min. The primer sequences used were GGTGAATACGTTCCCGG and TACGGCTACCTTGTTACGACTT.[5] Bacterial copy numbers were determined using standard curves constructed with DNA from *E. coli DH5α* as reference bacteria.[6] Concurrently, we utilized pure DEPC-treated water as a non-template control (NTC) during qPCR quantification assays.

The same experimental procedure was used to quantitatively analyze the abundance of *F. nucleatum*. The primer sequences for each assay were as follows: *F. nucleatum* gene forward primer, CAACCATTACTTTAACTCTACCATGTTCA; *F. nucleatum* genus reverse primer, ATTGACTTTACTGAGGGAGATTATGTAAAAATC.[7] *F. nucleatum* copies were determined using standard curves constructed with DNA of *F. nucleatum.*

The information of samples was provided in **Table S1**. Samples were collected, processed and sequenced according to standard procedure[8]. Briefly, frozen tissue samples (40-70 mg) were extracted with CTAB method. All negative controls were processed according to the same protocols. Different controls including sampling control, DNA extraction control and no-template PCR amplification control were included to account for the various sources of contamination from the hospital and laboratory environments as well as the different stages of handling and processing of the samples. 16S rRNA gene amplification and sequencing was carried out by amplifying 5 regions on the 16S rRNA gene in multiplex. The libraries were sequenced using the Illumina NovaSeq 6000 system. The resulting reads were demultiplexed, filtered and aligned to the five amplified regions based on the primers' sequences. To combine the read counts from these regions accurately, the Short Multiple

Regions Framework (SMURF) method was employed.[9] For reference, the GreenGenes database (May 2013 version, with some improvements) was used. To ensure the reliability of the data, a series of filters were applied to detect and eliminate any contamination, as described in reference.[8]

In vivo experiment

To evaluate the in vivo behaviors of *F. nucleatum* in mice, 2×10^6 4T1 cells were injected into the breast pad of female BALB/c mice on day -7. On day 0, when the volume of 4T1 tumors reached 50-100 mm^3, *F. nucleatum* was intravenously (i.v.) injected with a dose of 5×10^7 CFU, and the breast tumors, paracancerous tissue, normal breast tissue and other major organs were harvested for qPCR analysis 72 hours later.

To evaluate the in vivo antibacterial ability of Colistin-LipoFM, 2×10^6 4T1 cells were subcutaneously injected into female BALB/c mice on day -7. 1×10^7 CFU of *F. nucleatum* was intratumorally (i.t.) injected into tumors on day 0, the above mice were randomly divided into four groups: 1) Untreated; 2) Colistin (i.v.); 3) Colistin-Liposome (i.v.); 4) Colistin-LipoFM (i.v.). Free colistin, Colistin-Liposome, Colistin-LipoFM were i.v. injected with the colistin dose at 15 mg/kg on days 1, 3 and 5. On day 6, the tumors were collected for CFU counting.

To evaluate the in vivo antibacterial ability of Doxy-LipoFM, 2×10^6 4T1 cells were subcutaneously injected into female BALB/c mice on day -7. The bacteria, including *F. nucleatum* (2×10^6 CFU), *S. sanguis* (2×10^6 CFU), *S. xylosus* (2×10^6 CFU) and *E. faecalis* (2×10^6 CFU), were i.t. injected into the breast tumors on day 0. The bacteria-infected mice were randomly divided into four groups: 1) Untreated; 2) Doxy (i.v.); 3) Doxy-Liposome (i.v.); 4) Doxy-LipoFM (i.v.). Free Doxy, Doxy-Liposome, Doxy-LipoFM were i.v. injected with the Doxy dose at 15 mg/kg on days 1, 3 and 5. On day 6, the tumors were collected for CFU counting.

To evaluate the effect of *F. nucleatum* on chemotherapy, 2×10^6 4T1 cells were subcutaneously injected into female BALB/c mice on day -7. When the volume of 4T1 tumors reached 50-100 mm^3 on day 0, the mice were randomly divided into three groups: 1) Untreated; 2) 5Fu (i.p.); 3) 5Fu (i.p.) + *F. nucleatum* (i.t.). *F. nucleatum* was i.t. injected into tumors at a dose of 1×10^7 CFU on day 0, and 5Fu was intraperitoneally (i.p.) injected with the dose of 25 mg/kg on days 1, 3, 5, 7, 9, 11 and 13. Then, the volume of 4T1 tumors was monitored every other day, and mice were euthanized on day 14. Their tumors were imaged, weighed and collected for hematoxylin and eosin (H&E), terminal deoxynucleotidyl transferase dUTP nick end labeling (TUNEL), Cleaved Caspases 3 and LC3 staining. A similar experiment was conducted for the MDA-MB-231 tumor model, except that 2×10^6 MDA-MB-231 cells mixed with Matrigel (Corning 354248) were subcutaneously injected into female BALB/c-Nude mice on day -14. To evaluate the effect of OXA on the *F. nucleatum*-infected mouse breast tumor model, 2×10^6 4T1 cells were subcutaneously injected into female BALB/c mice on day -7. *F. nucleatum* was i.t. injected into tumors at a dose of 1×10^7 CFU on day 0, and OXA was i.p. injected with a dose of 4 mg/kg on days 1, 4 and 7.

To evaluate the therapeutic effect of Colistin-LipoFM to overcome *F. nucleatum*-induced chemoresistance, 2×10^6 4T1 cells were subcutaneously injected into female BALB/c mice on day -7. When the volume of 4T1 tumors reached 50-100 mm^3 on day 0, the mice were randomly divided into six groups: 1) Untreated; 2) 5Fu (i.p.); 3) 5Fu (i.p.) + *F. nucleatum* (i.t.); 4) 5Fu (i.p.) + *F. nucleatum* (i.t.) + free colistin (i.v.); 5) 5Fu (i.p.) + *F. nucleatum* (i.t.) + Colistin-Liposome (i.v.); 6) 5Fu (i.p.) + *F. nucleatum* (i.t.) + Colistin-LipoFM (i.v.). *F. nucleatum* was i.t. injected into each tumor with the dose of 1×10^7 CFU on day 0, 5Fu was i.p. injected with a dose of 25 mg/kg on days 1, 3, 5, 7, 9, 11 and 13, and free colistin, Colistin-Liposome, Colistin-LipoFM were i.v. injected with the colistin dose at 15 mg/kg on days 1, 3 and 5. The sizes of the tumors were measured every other day, and the mice were euthanized when their tumor volume reached 1,000 mm^3.

To evaluate the therapeutic effect of Doxy-LipoFM to overcome bacteria-induced lung metastasis. 2×10^6

4T1-luc cells were injected into the breast pads of BALB/c mice to establish an orthotopic breast tumor model on day -7. On day 0, the mice were randomly divided into three groups: 1) Untreated; 2) Bacteria (i.t.); 3) Bacteria (i.t.) + Doxy-LipoFM (i.v.). The bacteria including *F. nucleatum* (2×10^6 CFU), *S. sanguis* (2×10^6 CFU), *S. xylosus* (2×10^6 CFU) and *E. faecalis* (2×10^6 CFU) were i.t. injected into the breast tumors on day 0, Doxy-LipoFM was i.v. injected with the Doxy dose of 15 mg/kg on days 1, 3 and 5. The progression of lung metastases was monitored using an in vivo bioluminescence imaging system (Perkin Elmer). On day 18, the tumors and lungs of mice with different treatments were collected for H&E staining and homogenized for CFU counting.

To evaluate the therapeutic effect of Doxy-LipoFM in promoting combination chemotherapy in bacteria-infected orthotopic breast cancer. 4T1-luc cells (2×10^6) were injected into the breast pads of BALB/c mice to establish an orthotopic breast tumor model on day -7. On day 0, the mice were randomly divided into five groups: 1) Untreated; 2) Bacteria (i.t.); 3) CMF (i.p.); 4) CMF (i.p.) + Bacteria (i.t.); 5) CMF (i.p.) + Bacteria (i.t.) + Doxy-LipoFM (i.v.). The bacteria, including *F. nucleatum* (2×10^6 CFU), *S. sanguis* (2×10^6 CFU), *S. xylosus* (2×10^6 CFU) and *E. faecalis* (2×10^6 CFU), were i.t. injected into the breast tumors on day 0, Doxy-LipoFM was i.v. injected with the Doxy dose of 15 mg/kg on days 1, 3 and 5. For the CMF-treated groups, cyclophosphamide (CTX) and methotrexate (MTX) were i.p. injected with a dose of 100 mg/kg CTX and 20 mg/kg MTX on days 1 and 7, 5Fu was i.p. injected with a dose of 25 mg/kg on days 1, 3, 5, 7, 9, 11 and 13. The sizes of the primary tumors were measured every other day, and the progression of lung metastases was monitored using an in vivo bioluminescence imaging system every six days. On day 18, the mice were euthanized, and their tumors and lungs were collected for H&E, TUNEL and Ki67 staining.

Supplemental Reference

1. Wang, J., Li, P., Yu, Y., Fu, Y., Jiang, H., Lu, M., Sun, Z., Jiang, S., Lu, L., and Wu, M.X. (2020). Pulmonary surfactant–biomimetic nanoparticles potentiate heterosubtypic influenza immunity. Science *367*, eaau0810. 10.1126/science.aau0810.
2. Yu, T., Guo, F., Yu, Y., Sun, T., Ma, D., Han, J., Qian, Y., Kryczek, I., Sun, D., Nagarsheth, N., et al. (2017). Fusobacterium nucleatum Promotes Chemoresistance to Colorectal Cancer by Modulating Autophagy. Cell *170*, 548-563.e516. 10.1016/j.cell.2017.07.008.
3. Martin, F.E., Nadkarni, M.A., Jacques, N.A., and Hunter, N. (2002). Quantitative microbiological study of human carious dentine by culture and real-time PCR: association of anaerobes with histopathological changes in chronic pulpitis. J Clin Microbiol *40*, 1698-1704. 10.1128/jcm.40.5.1698-1704.2002.
4. Bullman, S., Pedamallu, C.S., Sicinska, E., Clancy, T.E., Zhang, X., Cai, D., Neuberg, D., Huang, K., Guevara, F., Nelson, T., et al. (2017). Analysis of Fusobacterium persistence and antibiotic response in colorectal cancer. Science *358*, 1443-1448. 10.1126/science.aal5240.
5. Song, X., Sun, X., Oh, S.F., Wu, M., Zhang, Y., Zheng, W., Geva-Zatorsky, N., Jupp, R., Mathis, D., Benoist, C., and Kasper, D.L. (2020). Microbial bile acid metabolites modulate gut RORγ+ regulatory T cell homeostasis. Nature *577*, 410-415. 10.1038/s41586-019-1865-0.
6. Iida, N., Dzutsev, A., Stewart, C.A., Smith, L., Bouladoux, N., Weingarten, R.A., Molina, D.A., Salcedo, R., Back, T., Cramer, S., et al. (2013). Commensal Bacteria Control Cancer Response to Therapy by Modulating the Tumor Microenvironment. Science *342*, 967-970. 10.1126/science.1240527.
7. Abed, J., Emgård, Johanna E.M., Zamir, G., Faroja, M., Almogy, G., Grenov, A., Sol, A., Naor, R., Pikarsky, E., Atlan, Karine A., et al. (2016). Fap2 Mediates Fusobacterium nucleatum Colorectal Adenocarcinoma Enrichment by Binding to Tumor-Expressed Gal-GalNAc. Cell. Host. Microbe. *20*, 215-225. 10.1016/j.chom.2016.07.006.

8. Nejman, D., Livyatan, I., Fuks, G., Gavert, N., Zwang, Y., Geller, L.T., Rotter-Maskowitz, A., Weiser, R., Mallel, G., Gigi, E., et al. (2020). The human tumor microbiome is composed of tumor type–specific intracellular bacteria. Science *368*, 973-980. 10.1126/science.aay9189.
9. Fuks, G., Elgart, M., Amir, A., Zeisel, A., Turnbaugh, P.J., Soen, Y., and Shental, N. (2018). Combining 16S rRNA gene variable regions enables high-resolution microbial community profiling. Microbiome *6*, 17. 10.1186/s40168-017-0396-x.